Starvation sensing by mycobacterial RelA/SpoT homologue through constitutive surveillance of translation

Yunlong Li[1#], Soneya Majumdar[2#], Ryan Treen[1,3#], Manjuli R. Sharma[2], Jamie Corro[1,3], Howard B. Gamper[4], Swati R. Manjari[2], Jerome Prusa[5], Nilesh K. Banavali[2], Christina L. Stallings[5], Ya-Ming Hou[4], Rajendra K. Agrawal[2,3*], Anil K. Ojha[1,3*]

1. Division of Genetics, Wadsworth Center, New York State Department of Health, Albany, NY 12208, USA
2. Division of Translational Medicine, Wadsworth Center, New York State Department of Health, Albany, NY 12237, USA
3. Department of Biomedical Sciences, School of Public Health, University at Albany, Albany, NY 12208, USA
4. Department of Biochemistry and Molecular Biology, Thomas Jefferson University, Philadelphia, PA 19107, USA
5. Department of Molecular Microbiology, Washington University in St. Louis School of Medicine, St. Louis, MO 63110, USA

[#]Equal contribution

*Correspondence: anil.ojha@health.ny.gov; rajendra.agrawal@health.ny.gov

Abstract:

The stringent response, which leads to persistence of nutrient-starved mycobacteria, is induced by activation of the RelA/SpoT homologue (Rsh) upon entry of a deacylated-tRNA in a translating ribosome. However, the mechanism by which Rsh identifies such ribosomes *in vivo* remains unclear. Here, we show that conditions inducing ribosome hibernation result in loss of intracellular Rsh in a Clp protease-dependent manner. This loss is also observed in non-starved cells using mutations in Rsh that block its interaction with the ribosome, indicating that Rsh association with the ribosome is important for Rsh stability. The cryo-EM structure of the Rsh-bound 70S ribosome in a translation initiation complex reveals unknown interactions between the ACT domain of Rsh and components of the ribosomal L7/L12-stalk base, suggesting that the aminoacylation status of A-site tRNA is surveyed during the first cycle of elongation. Altogether, we propose a surveillance model of Rsh activation that originates from its constitutive interaction with the ribosomes entering the translation cycle.

52 **Significance:**

53 Bacteria persist under nutrient starvation by activating RelA/SpoT homologue (Rsh), which
54 synthesizes a growth regulating alarmone, ppGpp. Rsh is activated specifically upon
55 recognizing a translation elongation complex with deacylated tRNA at the A-site. It is however
56 unclear how Rsh identifies such a complex in vivo. We show here that conditions inducing
57 ribosome hibernation in mycobacteria cause loss of intracellular Rsh, implying that association
58 with translating ribosomes is necessary for intracellular stability of Rsh. Using structural analysis
59 of Rsh-bound 70S translation initiation complex, we propose here that mycobacterial Rsh
60 identifies a Rsh-activating ribosomal complex by constitutively surveying the ribosome entering
61 the translation cycle at the early elongation stage.

62 **Introduction:**

63 The stringent response in bacteria is a programmed adaptation to nutrient starvation facilitated
64 by the secondary messengers, guanosine tetra- or penta-phosphates [collectively called
65 (p)ppGpp] (1-4). This response promotes long-term survival and persistence of mycobacteria
66 under various stresses including antibiotics (5-10). The primary function of (p)ppGpp is to
67 reprogram the global gene expression in cells either directly by binding to RNA polymerase (3,
68 11) or by binding to other cellular targets (12-14).

69 The level of (p)ppGpp is primarily regulated by a GDP/GTP pyrophosphokinase and a
70 GDP/GTP pyrophosphohydrolase, encoded either as two enzymes RelA and SpoT in β- and γ-
71 proteobacteria (3), or as a single protein called Rel in other species (15). Further insights into
72 the domain architectures of RelA/Rel and the mechanism of its activation have been obtained
73 from the structures of either the free enzyme or in complex with the ribosome, mRNA and A-
74 and P-site tRNAs (16-20). RelA/Rel has five distinct domains (Fig. 1A): i) N-terminal domain
75 possessing the (p)ppGpp synthase and hydrolase activities, ii) TGS (ThrRS, GTPase, SpoT)
76 domain that interacts with 3' CCA tail of deacylated-tRNA, iii) alpha helical domain (AHD), iv)
77 zinc-binding domain (ZBD) that contacts the A-site finger (ASF) on the 23S rRNA and S19 at
78 the inter-subunit interface, and v) the ACT domain (Aspartate Kinase, Chorismate and TyrA)
79 occupying a cavity in the large 50S ribosomal subunit (or LSU) (17-19). The interaction between
80 the TGS domain and 3' CCA tail of the deacylated-tRNA stabilizes the tRNA in a distorted state
81 at the A-site, called the A/R state, while pinning the domain against the small 30S ribosomal
82 subunit (or SSU) and extending the flexible catalytic N-terminal domain of RelA in an open and
83 active conformation (17-19).

84 The mechanism by which RelA finds a stalled ribosome complex in a nutrient starved
85 cell is unclear. In the currently adopted 'hopping model', diffusible RelA samples translation
86 elongation complexes and binds to a stalled ribosome with deacylated A-site tRNA in the A/R
87 state, and upon catalyzing (p)ppGpp synthesis the enzyme 'hops' to another stalled complex

88 (21-23). The hopping model further hypothesizes that an inactive RelA in non-starved cells
89 acquires a ribosome-free, closed conformation, in which the catalytic activity is autoinhibited by
90 the CTD, either through intermolecular (24-26) or intramolecular interactions (27-32). Winther et
91 al. further proposed that free cytosolic RelA in *E. coli* binds to deacylated-tRNA before binding
92 to the translating ribosome (22), although this model is challenged by the evidence of RelA
93 bound to the ribosome without any tRNA at the A-site (18). Moreover, single-molecule tracking
94 of RelA-fluorescent protein suggests constitutive association between RelA and ribosome in
95 non-starved *E. coli* cells (33). Recognizing these discrepancies, Takada et al. offered a refined
96 hopping model in *B. subtilis* in which activation of the stringent response appears to be initiated
97 by a weak interaction between Rel and the ribosome before the complex is stabilized by the
98 entry of deacylated-tRNA at the A-site, although they found RelA-ribosome interaction in *E. coli*
99 to be too weak to universally validate their model (23). These studies while revealing subtle
100 differences in the properties of RelA homologues across bacterial species, also underscore the
101 limitations of biochemical assays in modeling a highly dynamic *in vivo* interaction between the
102 stringent factor and the translation machinery.
103 Mycobacteria encode a single dual-function enzyme, RelA/SpoT homologue (henceforth
104 called Rsh), with both kinase and hydrolase activities located in distinct domains of the enzyme
105 (25, 26, 34-36). The optimal kinase activity of mycobacterial Rsh is observed in a Rsh Activating
106 Complex (RAC) comprising mRNA, deacylated-tRNA and the ribosome (37). The ribosome in
107 *Mycobacterium smegmatis* and *Mycobacterium tuberculosis* (Mtb) is remodeled under relatively
108 moderate zinc starvation, and subsequently targeted for hibernation under severe zinc
109 starvation (38, 39). Ribosome remodeling involves replacement of ribosomal proteins containing
110 the CXXC motif (called C+ r- proteins) with their paralogs without the motif (called C- r-proteins)
111 (38, 40). The C- ribosome is subsequently targeted for hibernation by mycobacterial protein Y
112 (Mpy), with assistance from a zinc-sensing protein called Mpy recruitment factor (Mrf) (38, 39).

113 A zinc-bound form of Mrf is sensitive to degradation by Clp protease, such that Mrf
114 accumulation increases with decreasing concentration of zinc (39).
115 Investigating the interplay between the stringent response and ribosome hibernation in
116 mycobacteria, we observed that interaction with the ribosome is necessary for the stability of
117 intracellular Rsh in non-starved cells. The structure of Rsh-bound 70S ribosome in a translation
118 initiation complex allows us to propose a new mechanism of starvation sensing by
119 mycobacterial Rsh, in which its activation arises from its unique interaction with the ribosome
120 entering the translation cycle.
121
122 **Results:**
123 *Mrf attenuates the stringent response in zinc-starved mycobacteria*
124 We tested how a zinc-limiting growth condition that induces ribosome hibernation in *M.*
125 *smegmatis* would impact ppGpp synthesis. After 96-hours of growth in high- or low-zinc
126 Sauton's medium, wild-type *M. smegmatis* cells were exposed for 3 hours to macronutrient
127 starvation in tris-buffered saline with Tween-80 (TBST) to induce the stringent response to a
128 measurable level (6). Rsh-dependent accumulation of ppGpp upon TBST starvation of the high-
129 zinc culture was significantly greater than the low-zinc culture (Fig. 1B). To distinguish the
130 contribution of macronutrient depletion from zinc limitation in TBST, we examined the stringent
131 response in cells from high-zinc cultures after exposure to metal-chelated or zinc-supplemented
132 TBST. Metal chelation did not impact the ppGpp synthesis, indicating that macronutrient
133 starvation in TBST was the primary inducer of the stringent response (Fig. 1C).
134 Interaction with ribosomes is critical for the stringent response (21), we therefore
135 hypothesized that the attenuated stringent response in low-zinc cultures was likely due to zinc-
136 responsive changes in the ribosome structure and/or function. We therefore analyzed the Rsh
137 occupancy on the ribosome in high- and low-zinc cultures. Rsh occupancy on the ribosomes
138 purified from low-zinc cells was significantly lower than that from high-zinc cells (Fig. 1D).

139 Unexpectedly, the difference in Rsh abundance on the ribosome correlated tightly with the
140 levels in the total cellular lysate (Fig. 1D). Moreover, lack of any other detectable smaller Rsh
141 isoforms (Fig S1) suggests total loss of intracellular Rsh. Together, figures 1B-D show that
142 physiological conditions developed during zinc starvation decreases the abundance of Rsh and
143 thus its interaction with the ribosome, thereby diminishing the stringent response.
144 We next investigated the effect of two zinc-responsive physiological changes in the
145 ribosome, remodeling and hibernation, in altered Rsh stability and Rsh-ribosome interaction.
146 The Zur-mediated C+ to C- remodeling of the ribosome induced by zinc starvation did not
147 impact the Rsh-ribosome interaction: Rsh occupancy on the ribosome from a high-zinc culture
148 of wildtype was comparable to Δ*zur* and a strain constitutively synthesizing C- ribosomes (Fig.
149 S2). To determine the effect of zinc-responsive ribosome hibernation on Rsh-ribosome
150 interaction, we analyzed the impact of Mpy recruitment factor (Mrf) on Rsh stability, activity, and
151 its occupancy on the ribosome. Mrf binds to SSU and facilitates inhibition of translation and
152 growth retardation upstream to Mpy recruitment to the ribosome (39). In zinc-starved *M.*
153 *smegmatis,* deletion of *mrf* restored the levels of intracellular and ribosome-bound Rsh similar to
154 those in high-zinc wildtype cells, and the mutant phenotype was complemented by plasmid-
155 borne *mrf* (Fig. 2A-B). The increase in Rsh abundance in zinc-starved Δ*mrf* also correlated with
156 the increase in ppGpp levels upon exposure to TBST (Fig. 2C). Together, these data suggest
157 that: i) the limiting intracellular free zinc concentration has little direct impact on the stringent
158 response, and ii) accumulation of Mrf induced by zinc depletion and likely downregulation of
159 translational activity decrease total Rsh abundance in the cell. Deletion of *rsh* did not impact
160 Mpy-ribosome interaction (Fig. S3), distinguishing mycobacteria from other species in which
161 ppGpp transcriptionally induces factors necessary for ribosome hibernation (41-43).
162
163 *Ectopic expression of Mrf can reduce intracellular abundance of Rsh.*

164 To further establish the relationship between Rsh abundance and Mrf accumulation, we
165 examined the impact of an ectopic expression of a Mrf variant (Mrf*) on Rsh levels in zinc-rich
166 cells. Mrf* has reduced zinc affinity and is recalcitrant to regulation by the Clp protease system
167 (39). Consequently, constitutive expression of Mrf* leads to its substantial accumulation in high-
168 zinc mycobacteria (39), presumably in a conformation that is capable of binding to the ribosome
169 and inhibiting both translation and cellular growth. The abundance of Rsh and its association
170 with the ribosome was determined upon acetamide-inducible expression of Mrf* in high-zinc
171 cultures of *M. smegmatis*. Figure 2D shows that the expression of Mrf* in high-zinc cells led to
172 concomitant loss of Rsh, both in the lysates (Fig. 2D) and on the ribosomes (Fig. 2E).
173 Because SpoT in *Salmonella enterica* was identified as a potential substrate of the Clp
174 protease system (44), we tested the possibility whether mycobacterial ClpP1P2 protease could
175 be involved in regulating the abundance of free Rsh in cells. We used a *M. smegmatis* strain,
176 which constitutively transcribed FLAG-tagged Mrf and harbored an anhydrotetracycline-
177 inducible CRISPR-Ca9 system for targeting ClpP1 (39), to test whether Rsh loss during Mrf
178 stabilization is Clp-dependent. Depletion of ClpP1 in high-zinc cells resulted in concomitant
179 accumulation of both Mrf and Rsh (Fig. 2F). Thus, loss of Rsh in cells during Mrf stabilization is
180 likely achieved through a Clp-dependent mechanism, although whether Rsh is a direct substrate
181 of Clp remains unknown.
182
183 *Interaction with the ribosome is necessary for intracellular stability of Rsh*
184 Above, we have established loss of Rsh in cells with progressively increasing amounts of Mrf
185 prior to ribosome hibernation, suggesting that availability of translating ribosome might be
186 important for Rsh stability. Moreover, similar levels of Rsh-bound ribosomes in high-zinc
187 cultures before and after nutrient starvation (Fig. S4), suggesting that there is a constant level of
188 Rsh-ribosome interaction regardless of the changes in the relative levels of (p)ppGpp. We
189 therefore tested whether interaction with the ribosome impacts the intracellular stability of Rsh.

190 *E. coli* RelA interacts with the ribosome primarily through its CTD containing a conserved CCHC
191 type zinc-finger in the ZBD, which makes extensive contacts with the inter-subunit region of the
192 70S ribosome, and ASF of the LSU (17, 45). Although the requirement of zinc in RelA-ribosome
193 interaction remains unclear, the zinc coordinating residues C612, C613, H634 and C638 (C666,
194 C667, H688 and C692 in *M. smegmatis Rsh*) of ZBD are conserved in mycobacteria and likely
195 acquire the same three-dimensional conformation as in *E. coli* RelA (Fig. 3A). Furthermore,
196 mutation of C633 in *M. tuberculosis* Rsh (C692 in *M. smegmatis*) impairs the enzyme *in vitro*
197 (25), supporting an important role of this residue in the Rsh activity. We therefore mutated the
198 key ZBD residues and studied the impact on the intracellular abundance of Rsh. The mutation
199 scheme closely mirrored the previous study (24), which also showed that mutation in the
200 neighboring D637 (D691 in *M. smegmatis*) had substantially less impact on protein function
201 compared to C638 (C692 in *M. smegmatis*). Substitution of C666 and C692 residues resulted in
202 substantial loss of Rsh in both the cell lysate and on the ribosome in actively growing *M.*
203 *smegmatis* cells in zinc-rich conditions (Fig. 3B). The presence of wildtype Rsh on the ribosome
204 was unambiguous (Fig. 3B), supporting the notion that Rsh-ribosome interaction in non-starved
205 cells is constitutive. Substitution in the adjacent D691 neither impacted the Rsh-ribosome
206 interaction nor the intracellular abundance of the protein (Fig. 3B). Recombinant expression of
207 these Rsh variants in *E. coli* did not significantly impact the protein yield (Fig. S5), indicating that
208 these mutations do not affect the intrinsic stability of the protein *in vivo*, and their properties are
209 likely determined by the intracellular environment of mycobacteria. To further test if the
210 mutations specifically disrupted Rsh-ribosome interaction in mycobacteria, we mixed
211 recombinant Rsh_{C666G} and Rsh_{C692F} variants with 70S ribosomes purified from Δ*rsh* mutant of *M.*
212 *smegmatis* and analyzed their occupancy on the ribosome. Ultracentrifugation on a 32%
213 sucrose cushion was used to separate ribosome-bound from unbound Rsh. Compared to the
214 wildtype Rsh, association with the ribosome was significantly compromised for both
215 recombinant proteins, Rsh_{C666G} and Rsh_{C692F} (Fig. 3C). We thus conclude that Rsh constitutively

216 interacts with the ribosome using its ZBD in non-starved cells, and this interaction is necessary
217 for the intracellular stability of the enzyme.
218
219 *Rsh interacts with the IF2 bound 70S initiation complex*
220 We next focused on understanding the stage of translation when Rsh would most likely interact
221 with the ribosome in a non-starved cell. We streamlined our approach based on the published
222 structures (17-19), which delineate permissive and non-permissive translation complexes for
223 RelA binding. While RelA can bind to a late translation-initiation intermediate (70S- fMet-
224 $tRNA_i^{Met}$ -mRNA with vacant A-site) (18), its binding to the ribosome during translation
225 elongation is expected to be sterically hindered by inter-subunit rotation (17-19). We therefore
226 hypothesized that mycobacterial Rsh would enter the translation initiation complex through one
227 of the free ribosomal subunits and likely remain on the complex until the start of the first cycle of
228 elongation. This hypothesis also implies that Rsh must remain associated with the ribosome
229 during its transition from initiation to pre-elongation stages, without affecting the overall
230 canonical conformation of the translation complex.
231 To investigate this possibility, we first determined the propensity of Rsh to interact with
232 free ribosomal subunits. Purified recombinant Rsh was mixed individually with each of the two
233 purified ribosomal subunits free of any canonical protein synthesis ligands and the
234 macromolecules were separated on a 32% sucrose cushion. Rsh appeared to preferentially co-
235 sediment with the LSU (Fig. 4A). We next asked if Rsh would remain in the translation complex
236 during its transitions through the various intermediate stages of initiation, especially given the
237 potential of a steric clash between Rsh and translation initiation factor 2 (IF2). The contact
238 points of IF2 on the 70S initiation complex significantly overlaps with those of Rsh (17-19, 46).
239 We therefore tested the ability of Rsh to interact with the ribosome in the presence of IF2, fMet-
240 $tRNA_i^{Met}$ and mRNA *in vitro*. Dissociated ribosomes (Fig. S6) were mixed with His_6-IF2, His_6-
241 Rsh, fMet-$tRNA_i^{Met}$, leadered mRNA, and either GTP or a non-hydrolysable analogue (GMP-

242 PNP). The assembled 70S complex purified on 10-40% sucrose density gradient (SDG) was
243 analyzed for the presence of IF2 and Rsh. The 70S ribosomes assembled in the presence of
244 GTP contained Rsh but had undetectable levels of IF2 (Fig. 4B), demonstrating that Rsh can
245 associate with the ribosome in the presence of the canonical ligands without interfering with
246 GTP-dependent release of IF2 (47). This property of mycobacterial Rsh is in sharp contrast to
247 *B. subtilis* Rel, which cannot form a stable complex with the ribosome without an A-site
248 deacylated-tRNA (23). Unexpectedly, both Rsh and IF2 were detected in 70S particles
249 assembled in the presence of GMP-PNP (Fig. 4C), suggesting that one or both proteins could
250 be occupying the ribosome in their non-canonical states.
251
252 *Cryo-EM structure reveals unknown ribosome-Rsh interactions*
253 To gain further insight into the Rsh-bound *M. smegmatis* 70S ribosome in a translation initiation
254 complex, we performed single-particle cryo-EM to determine the structure of the 70S ribosome
255 assembled in the presence of IF2, Rsh, fMet-tRNA$_i^{Met}$, leadered mRNA, and GMP-PNP. 3D
256 classification of the cryo-EM dataset (Figs. S7, S8, Table S3) revealed a unique class of Rsh-
257 bound ribosome in a classical non-rotated state, but none of the classes showed any density for
258 IF2. The Rsh-bound 3D class refined to 2.7 Å resolution showed densities only for two C-
259 terminal domains of Rsh, ZBD and ACT, along with a fMet-tRNA$_i^{fMet}$ bound at the ribosomal P
260 site, while all other domains were found to be disordered (Figs. 4D, 4E, S7 and S9). The ZBD
261 interacts with both the SSU and LSU: specifically, protein uS19 of the SSU and 23S rRNA helix
262 H38 of the LSU (also referred to as ASF) (Fig. 4E). These interactions resemble those reported
263 in the structures of *E. coli* RelA and *B. subtilis* Rsh on the ribosome (18, 20). The Rsh-ACT
264 domain occupies the inter-subunit space and interacts with LSU proteins uL16, uL11, and the
265 23S rRNA helices H43-44 at the base of the protein L7/L12 stalk (Fig. 4E).
266 Previous structural studies suggest IF2 and RelA binding to the ribosome would be
267 mutually exclusive (18, 46). However, our data shows co-existence of the two proteins in a

268 reconstituted 70S translation initiation complex (Fig. 4C). To begin to resolve this issue, we
269 superimposed either our mycobacterial structure or the *E. coli* 70S ribosome-RelA structure (18)
270 with 70S-IF2-GMP-PNP initiation complexes (46). Indeed, RelA's alpha-helical domain (AHD)
271 would directly clash with domain VI-C1 of IF2 (Fig. 4F). In tertiary structure, the AHD of *E. coli*
272 RelA lies adjacent to the ACT domain while the ZBD is anchored to the ribosome via its
273 interactions with uS19 and ASF (18). In our structure the rotational angle between the ACT and
274 ZBD domains was ~14 degrees greater than that in *E. coli* RelA (Fig. 4F) and AHD was
275 disordered, presumably displaced from its canonical position, thus avoiding a clash with domain
276 VI-C1 of IF2 (Fig. 4F). The ACT domain is known to exhibit some conformational variations with
277 respect to the ZBD domain in the previously published structures (18, 20), but an additional
278 rotation by 14 degrees is unprecedented. It is possible that the adopted conformation of the ACT
279 domain in our structure is to accommodate the exiting IF2 molecule upon completion of the
280 translation initiation phase.

281 Compared to the *E. coli* RelA and *B. subtilis* Rel, mycobacterial Rsh shows an overall
282 similarity in tertiary structures of ZBD and ACT domains, although the rotation of the ACT
283 domain translates into its shift by ~6 Å towards the LSU's L7/L12 stalk base (Fig. 5A, B). This
284 altered conformation of ACT in Rsh is stabilized through extensive interactions with the uL11
285 and the 23S rRNA helices H43/44 (Fig. 5C). Specifically, uL11 lysines, 89 and 96 interact with
286 Y791, D789 and H776 of Rsh-ACT. Further, Rsh-ACT S779, N783, D789 and Y788 interact with
287 the 23S rRNA helices H43-44 phosphate backbones. These interactions are in sharp contrast to
288 the *E. coli* ribosome-RelA structures, where uL11 interacts with the A/R tRNA but not directly
289 with RelA (18). Thus, our structure reveals a unique conformational state of the ribosome-bound
290 Rsh. Multiple sequence alignment of the amino acid sequences does not reveal any apparent
291 substitutions, insertions, or deletions that can explain the altered orientation of the ACT domain
292 in *M. smegmatis* Rsh (Fig. S10). Given that our structure was obtained in the presence of IF2-

293 GMP-PNP, a key difference from the *E. coli* ribosome-RelA complex, a possible role of IF2 in
294 inducing the rotation of ACT cannot be ruled out.
295 Interactions stabilizing Rsh in mycobacterial structure are primarily through LSU's ASF,
296 uL16, uL11, and rRNA helices H43/44, suggesting that Rsh associates primarily with the LSU,
297 corroborating the results of our binding experiments that show association of Rsh with free LSU.
298 The rRNA helices H43/44 and uL11 together constitute the L7/L12-stalk base of LSU and are
299 known to be mobile during elongation (48) and recycling (49) phases of translation. We thus
300 propose that intensive contacts between the L7/L12-stalk base and the Rsh-ACT domain would
301 transiently lock the ribosome in a stalled state before the start of the translation elongation
302 cycle, as a mechanism to survey the aminoacylation state of the incoming tRNA to the A site. A
303 direct contact of Rsh with uL11 is distinct from *E. coli* RelA, which binds to the ribosome in
304 uL11-independent manner, even though uL11 and a deacylated-tRNA at the A-site are required
305 for (p)ppGpp synthesis (21, 50-52). While the structural changes in *M. smegmatis* complex here
306 could be induced by the presence of IF2, we cannot exclude the possibility that these are
307 intrinsic *to M. smegmatis* Rsh.
308 The superimposed structures also reveal some species-specific differences in
309 Rsh/RelA/Rel, which could probably explain differences in their ribosome binding affinities (Fig.
310 S10). The ZBD domains interact with uS19 and ASF in all three cases, however, compared
311 to *M. smegmatis*, *B. subtilis* Rel has additional interactions — two with uS19, one with ASF, and
312 one with uS13 (Fig. S10). The loss of the additional interactions with uS19 and ASF in *M.*
313 *smegmatis* is likely due to substitution at corresponding positions with non-polar amino acids
314 (Fig. S10). However, *M. smegmatis* Rsh-ZBD could potentially interact with uS13 since it has an
315 Arg (R681) corresponding to K617 in *B. subtilis*. The *E. coli* RelA ZBD also has two additional
316 interactions compared to *M. smegmatis*, one with uS19 and the other with ASF (Fig. S10).
317 However, *E. coli* RelA ZBD has a Gln (Q627) corresponding to K617 and R681 in *B.*
318 *subtilis* and *M. smegmatis*, respectively, which might not interact with uS13 due to its shorter

319 side chain. Since the density corresponding to ZBD is relatively strong in our structure, we
320 designate it as the primary anchoring domain of mycobacterial Rsh.
321
322 *Exclusion of Rsh from Mpy-bound ribosomes*
323 The requirement of the ribosomes for the intracellular stability of Rsh, combined with its loss in
324 cells harboring Mrf and Mpy-bound hibernating ribosomes, suggests that Rsh is not able to bind
325 to hibernating ribosomes. Mpy and Rsh bind at two physically distinct sites on the unrotated
326 SSU of the ribosome (Fig. 6A). The Mpy N-terminal domain binds to the SSU spanning the
327 decoding center by interacting extensively with the 16S rRNA components that converge from
328 platform, body, and head regions at the SSU's neck (38). By contrast, the Rsh ZBD interacts
329 near the inter-subunit bridge B1a (53) forming components, including uS19 of the SSU and the
330 LSU's ASF (54) (Figs. 4E and 6A). Since the binding sites of the two factors do not overlap, we
331 superimposed the structures of Rsh- and Mpy-bound *M. smegmatis* 70S ribosomes to
332 understand the accessibility of Mpy-bound hibernating ribosome to Rsh binding. Both the
333 ribosomes are in an unrotated state, but the SSU head domain in the Rsh-bound structure is
334 tilted more towards the LSU in comparison to the Mpy-bound ribosome structure (Fig. 6B). We
335 predict that the untilted SSU head in the MPY-bound state will prevent stable interactions
336 between Rsh-ZBD and uS19 (Fig. 6C). ZBD is the primary anchoring domain of Rsh (18, 20),
337 thus, any alteration in the bridge B1a configuration in the Mpy-bound state is likely to directly
338 inhibit Rsh binding, thereby rendering ribosome-free labile Rsh. Thus, reduction in the
339 intracellular Rsh during ribosome hibernation could be a combined outcome of both a decrease
340 in the synthesis of new Rsh and the occlusion of pre-existing Rsh from the hibernating
341 ribosome.
342
343 **Discussion:**

344 The stringent response, characterized by Rsh-dependent synthesis of (p)ppGpp and
345 subsequent transcriptional reprogramming by the alarmone, is among the central adaptation
346 mechanisms in nutrient-starved mycobacteria. Yet, a significant knowledge gap exists in the
347 mechanism underlying starvation sensing by Rsh. Structural studies with *E. coli* RelA provide
348 mechanistic details on how Rsh is activated by the presence of deacylated-tRNA at the A- site
349 in a stalled translation-elongation complex. However, it remains unclear how Rsh would
350 encounter such a complex *in vivo*. Two models have emerged from recent studies: a) the
351 hopping model in which a Rel-deacylated-tRNA complex is formed prior to its entry at the A- site
352 of the elongation complex (22), and b) starvation-induced formation of a weak RelA-ribosome
353 complex prior to its stabilization by deacylated-tRNA (23). Both models however preclude RelA-
354 ribosome interaction in non-starved cells, which is inconsistent with the evidence of constitutive
355 RelA-ribosome interaction throughout the growth of *E. coli* and *P. aeruginosa* cells (33, 55).
356 Here, we propose a new model of Rsh recognition of a stalled translation complex in
357 mycobacteria. In this model, which we call the surveillance model, Rsh constitutively interacts
358 with ribosomes during the formation of the initiation complex, and its transition to the pre-
359 elongation stage (Fig. 7A). Consequently, entry of an amino acylated-tRNA would allow
360 elongation, accompanied by inter-subunit rotation that would displace Rsh from the complex
361 (Fig. 7B) (17-19). By contrast, entry of a deacylated tRNA into the A-site would trigger Rsh
362 activation and (p)ppGpp synthesis (Fig. 7D). Free Rsh appears to be labile (Fig. 7G). To
363 maintain steady state levels Rsh must therefore associate with free LSU entering the translation
364 cycle (Fig. 7C), or another stalled elongation complex with deacylated-tRNA at the A- site (Fig.
365 7E). The latter interaction is expected to be uncertain and less frequent given the low
366 abundance of stalled elongation complexes relative to large abundance of free LSU. Given that
367 Rsh abundance in an actively growing cell is ~200-fold less compared to the ribosome (21), a
368 rapid rate of translation would likely maintain a sufficiently large pool of free LSU transitioning
369 between termination and initiation cycles, thereby ensuring a stable population of Rsh-ribosome

370 complex. The predictable fates of Rsh in the surveillance model renders the model more
371 stringent than either the original or the refined hopping model, both of which rely on random
372 encounter of Rsh with a deacylated-tRNA and/or a stalled ribosome.

373 The lack of Rsh under conditions such as those inducing ribosome hibernation further
374 supports the model that optimum protein synthesis and accessibility to LSU entering the
375 translation cycle is critical for the intracellular stability of Rsh (Fig. 7F). This loss of Rsh further
376 differentiates the physiological conditions for ribosome hibernation and the stringent response.
377 The stringent response is an upstream response before ribosome hibernation; a logical order
378 given that the stringent response reprograms gene expression to fine-tune metabolism, while
379 ribosome hibernation directly shuts down global protein synthesis. Moreover, restoration of
380 (p)ppGpp synthesis in a zinc-depleted Δ*mrf* strain implies that Rsh-ribosome interaction and
381 Rsh activation are relatively less sensitive to intracellular depletion of free zinc. We hypothesize
382 that the coordinating zinc residues of Rsh have high affinity for zinc, supporting continued
383 interaction with the ribosome even during the declining intracellular level of free zinc. This would
384 allow activation of Rsh under low-zinc conditions before the induction of Mpy-dependent
385 ribosome hibernation.

386 Zinc is an essential nutrient that binds to 6-10% of all proteins in bacteria (56). Notably,
387 several amino acyl tRNA synthetases are zinc binding proteins (56). A lack of zinc in the active
388 site of threonyl-tRNA synthetase inactivates the aminoacylation activity of the enzyme (57).
389 Moreover, after alanine (26%) threonine (17%) is the second-most frequent amino acid to follow
390 the initiator Met in the top 183 most translated genes in *M. smegmatis*. Limitation in zinc
391 therefore will directly increase the level of deacylated-Thr-tRNA, activating the stringent
392 response through the surveillance model. Thus, the intracellular availability of zinc in
393 mycobacteria could potentially be a shared signal for the sequential onset of the stringent
394 response and ribosome hibernation, mediated directly through sensing the translation activity of
395 the ribosome. Beyond zinc starvation as the documented condition leading to mycobacterial

396 ribosome hibernation, it is likely that other conditions inducing ribosome hibernation would also
397 attenuate the stringent response in a similar manner.
398 The Clp-dependent loss of ribosome-free intracellular Rsh, while unveiling a novel
399 mechanism of regulation of Rsh activity *in vivo*, does not entirely rule out the CTD-dependent
400 autoinhibition of the synthase activity through oligomerization: a model primarily proposed from
401 *in vitro* characterization of the enzyme (24-26). However, the evidence of ribosome-bound Rsh
402 as the dominant species *in vivo* suggests that Rsh oligomers, if any, would be a relatively minor
403 molecular species in the cell. The predominance of ribosome-bound Rsh *in vivo* further
404 suggests a reversible transition between the synthase and the hydrolase activities may occur
405 through differential allosteric effects of ppGpp and GDP/ATP binding to the hydrolase and the
406 synthase domain, respectively, as shown by Tamman et al. (28).
407 In summary, we propose a unique structure-based mechanism of mycobacterial Rsh
408 recognition of translating ribosomes stalled with deacylated A-site tRNA, in which the enzyme
409 predominantly surveys the amino acylation status of the tRNA during the first cycle of elongation
410 to activate the stringent response. This mechanism of Rsh activation is programmed to slow
411 down upon induction of ribosome hibernation. These findings will serve as a new molecular
412 frame of reference for further investigation of the relationship between the stringent response
413 and ribosome hibernation in mycobacteria.
414

415 **Materials and Methods:**

416 **Bacterial growth medium**

417 *Mycobacterium smegmatis* (mc^2155) and its variant strains were grown shaking at 200 rpm at 37
418 °C in Middlebrook 7H9 with ADC enrichment (5% albumin, 2% dextrose, 0.85% sodium chloride
419 and 0.003% catalase) and 0.05% (v/v) Tween80. For ribosome purification, cells from saturated
420 cultures were washed with PBS + 0.05% (v/v) Tween80 for three times and then inoculated at
421 1:100 dilution in Sauton's medium with either 1 mM $ZnSO_4$ for high-zinc condition or 1 μM zinc-
422 chelator (TPEN, N,N,N',N'-Tetrakis(2-pyridylmethyl)ethylenediamine) for low-zinc condition.
423 7H10ADC agar plate was used for selection of recombinants and colony growth (*M. smegmatis*).
424 *Escherichia coli* (GC5 or BL21) was grown in LB broth or LB agar at 37 °C. Zeocin (25 μg/mL),
425 kanamycin (20 μg/mL), hygromycin (150 μg/mL for *M. smegmatis* and *E. coli*, carbenicillin (50
426 μg/mL), and apramycin (5 μg/mL) were used for selection as necessary. For recombinant strain
427 harboring acetamide-inducible promoter, cells were cultured in high- or low -zinc Sauton's
428 medium with 0.2% sodium succinate and induced with 0.2% acetamide.

429

430 **Construction of recombinant plasmids and strains**

431 A list of plasmids, bacterial strains used in this study is provided in Table S1. A list of
432 oligonucleotides used in this study is provided in Table S2. For construction of Δ*rsh* in *M.*
433 *smegmatis*, the gene was replaced with a zeocin-resistance marker using a PCR-based modified
434 version of the recombineering strategy as previously described (38). For creating $C_{666}G$, $D_{691}R$
435 and $C_{692}F$ variants of Rsh, the Rsh ORF with 500 bp of upstream sequence was PCR-amplified
436 and cloned between KpnI and XbaI sites of the integrative vector pMH94 (39), resulting in the
437 recombinant plasmid pYL238. Mutations at the respective sites were introduced using pYL238 as
438 a template by PCR-based mutagenesis using the primer pairs listed in Table S2, resulting in
439 pYL240 ($C_{666}G$), pYL241 ($D_{691}R$) and pYL242 ($C_{692}F$). Mutations were sequence-confirmed and

440 the plasmids pYL238, pYL240, pYL241 and pYL242 were electroporated into the mc^{2}155:Δ*rsh*
441 strain of *M. smegmatis*. Cells expressing the mutant variants were cultured in nutrient-rich
442 medium and analyzed for Rsh levels by immunoblotting. The integrative plasmid with
443 anhydrotetracycline(ATc)-inducible CRISPRi-dCas9 system targeting the *clpP1* expression was
444 constructed and donated by Dr. Keith Derbyshire as a part of the Mycobacterium Systems
445 Resources (MSR)(58). The *M. smegmatis* strain (YL9) harboring the plasmid was cultured in high-
446 and low-zinc and ClpP1 depletion was induced by ATc as described previously (39).
447
448 **Recombinant protein expression and purification**
449 Rsh from *M. smegmatis* (Msmeg_2965) and its variants (Rsh_{C666G}, Rsh_{D691R} and Rsh_{C692F}) with an
450 N-terminal His tag fusion were subcloned in pET21b vector using NdeI and HindIII. The plasmids
451 were introduced into BL21 (DE3) pLysS cells for Rsh expression and purification. Briefly, the cells
452 were grown in LB medium to log phase (OD_{600} of 0.7) at 37 °C, when RSH expression was induced
453 with 0.5 mM IPTG for 4 hours at 37 °C. Induced cells were harvested (8000 rpm, 20 minutes at 4
454 °C in Thermo Scientific™ Fiberlite™ F12-6 × 500 Fixed-Angle Rotor) and then resuspended in N-
455 I buffer (50 mM Tris (pH 8.0), 300mM NaCl, 5% glycerol, 10 mM imidazole, 1mM PMSF). The
456 cells were further sonicated (Amplitude 30%, 6 cycles of 10 sec on and 60 sec off for) at 4 °C and
457 the soluble protein in the supernatant was separated from the debris by centrifugation (13000
458 rpm, 20 minutes, 4 °C in Thermo Scientific™ Fiberlite™ F12-6 × 500 Fixed-Angle Rotor) and
459 incubated with pre-equilibrated Ni-NTA resin for 1 hour at 4 °C. After incubation, Ni-NTA resin
460 was washed three times with N-II buffer [50 mM Tris (pH 8.0), 300mM NaCl, 5% (v/v) glycerol, 30
461 mM imidazole]. Rsh was then eluted with stepwise increments of imidazole (from 60 mM, to
462 100mM and to 250 mM) in a buffer containing 50 mM Tris (pH 8.0), 300mM NaCl and 5% (v/v)
463 glycerol. Peak fractions with were pooled and imidazole was removed by dialysis in the buffer
464 containing 50 mM Tris (pH 8.0), 300mM NaCl and 30% (v/v) glycerol. For recombinant IF2

465 (MSMEG_2628) with N-terminal His_{6x} tag, the full-length codon optimized gene with N-terminal
466 6x-His-sequnce and NdeI-XhoI sites was synthesized (IDT DNA Inc.) (Table S2). The synthetic
467 fragment was cloned into a pET21a vector. Recombinant protein was expressed in BL21-DE3
468 (pLysS) and purified on Ni-NTA matrix as detailed for His_6-Rsh above.
469
470 **Ribosome purification**
471 Rsh bound ribosomes were purified with a few modifications from the previously described
472 protocol (38). *M. smegmatis* cells were grown for the specified time in 500 mL of Sauton's media
473 containing 0.05% Tween 80 and either 1 mM $ZnSO_4$ or 1 μM TPEN. Cells were harvested (8000
474 rpm for 20 minutes in a Thermo Scientific™ Fiberlite™ F12-6 × 500 Fixed-Angle Rotor) and
475 pulverized 6 times at 15 Hz for 3 minutes in a mixer mill (Retsch MM400). The lysates were mixed
476 with 20 mL of HMA-10 buffer (20 mM HEPES-K pH7.5, 30 mM NH_4Cl, 10 mM $MgCl_2$, 5 mM β-
477 mercaptoethanol) and centrifuged for 30 minutes at 30,000g in Thermo Scientific™ Fiberlite™
478 F12-8 × 50 Fixed-Angle Rotor. The supernatants were collected in the Beckman PC
479 ultracentrifuge tubes and further centrifuged for 2 hours and 15 minutes at 42800 rpm in a
480 Beckman rotor Type 70Ti. Pellets were soaked in 4 mL of HMA-10 buffer in an ice water bath
481 overnight, and then homogenized for 30 minutes. The homogenized pellets were treated with 3
482 units/mL Rnase-free Dnase (Ambion) for two hours at 4 °C. The contents were transferred to
483 Beckman PA tubes and centrifuged at 22,000 g for 15 minutes in Thermo Scientific™ Fiberlite™
484 F12-8 × 50 Fixed-Angle Rotor. The supernatants were collected into Beckman ultracentrifuge PC
485 tubes and centrifuged for 2 hours and 15 minutes at 42,800 rpm in a Beckman rotor Type 70Ti.
486 The pellets were dissolved in 1 mL HMA-10 buffer and centrifuged for 10 minutes at 10,000 g.
487 The supernatants containing the crude ribosomes were collected and quantified by measuring
488 their optical density at 260 nm. The crude ribosome preparations were then layered on top of 37
489 mL sucrose density gradients (10%-40%) and centrifuged for 16 hours at 24,000 rpm in a
490 Beckman rotor SW 28. The 70S ribosome fractions were collected after fractionating the sucrose

491 gradient in a 260 nm Brandel gradient analyzer as previously described (59). The pooled 70S
492 ribosome fractions pelleted by ultracentrifugation at 42,800 rpm for 3 hours in a Beckman rotor
493 Type 70Ti were suspended in HMA-10 buffer (20 mM HEPES-K pH7.5, 30 mM NH_4Cl, 10 mM
494 $MgCl_2$, 5 mM β-mercaptoethanol) and quantified by measuring absorbance at 260 nm.

495 MPY-bound ribosomes and other high-salt washed ribosomes were purified exactly as
496 described previously (38, 39). The steps up to homogenization were same as described above.
497 After homogenization, 4 mL of the homogenized suspension was treated with 3 units/mL Rnase-
498 free Dnase (Ambion) for one hour at 4 °C, then 4 mL of HMA-0.06 buffer (20 mM HEPES-K pH
499 7.5, 600 mM NH_4Cl, 10 mM $MgCl_2$, 5 mM β-mercaptoethanol) was added to the suspension, which
500 was further incubated at 4 °C for 2 hours. The content was transferred to Beckman PA tubes and
501 centrifuged at 22,000 g for 15 minutes in Thermo Scientific™ Fiberlite™ F12-8 × 50 Fixed-Angle
502 Rotor. Supernatants were collected and layered on top of 8 mL 32% sucrose solution in HMA-10
503 buffer and centrifuged for 16 hours at 37000 rpm in a Beckman rotor Type 70Ti. The supernatant
504 was discarded, and the pellet was rinsed with HMA-10 buffer to remove the brownish material.
505 The crude ribosome was resuspended in 1 mL HMA-10 buffer and centrifuged for 10 minutes at
506 10,000 g. Supernatant containing the crude ribosome was collected and quantified by measuring
507 optical density at 260nm. 70S ribosome from the crude ribosome was further separated on a 10-
508 40% sucrose density gradient and fractionated as indicated above.

509

510 **In vitro reconstitution of Rsh with 70S initiation complex**

511 *Co-sedimentation of Rsh with the ribosomal subunits:* 70S ribosomes were purified from low-zinc
512 culture of isogenic Δ*rsh*/Δ*mpy*/Δ*mrf* triple mutant of *M. smegmatis*. Subunits were dissociated from
513 the purified 70S ribosomes by incubation at 37°C for thirty minutes in HMA-1 buffer (20 mM
514 HEPES-K pH7.5, 30 mM NH_4Cl, 1 mM $MgCl_2$, 5 mM β-mercaptoethanol. The resulting subunits

515 were then purified from a 10-40% sucrose density gradient. Individual subunits equivalent to A_{260}
516 of 0.3 (7.2 pmol) were mixed with 1.8 pmol of purified recombinant Rsh in 100 μL binding buffer
517 (20 mM HEPES-K pH7.5, 100 mM NH4Cl, 10 mM $MgCl_2$, 5 mM β-mercaptoethanol, 50mM KCl),
518 and the mixture was incubated for thirty minutes at 37°C. The reactions were then layered on 100
519 μL of 32% sucrose cushion and centrifuged at 42,800 rpm for 3 hours in a Beckman TLA 100
520 rotor using the Optima-Max TL ultracentrifuge (Beckman Coulter). After centrifugation, the
521 supernatant was discarded, and the ribosome pellet was resuspended in 20 μL HMA-10 buffer.
522 The abundance of Rsh was further determined by immunoblotting using the protocol described
523 below Rsh, and S13, and L33.
524 *Preparation of fMet-tRNA$_i^{Met}$:* An *E. coli* culture containing a plasmid borne expression vector for
525 tRNA$_i^{Met}$ under control of the LacI repressor was grown to an optical density at 600 nm of 0.4-
526 0.6 at which time IPTG was added to induce expression of the tRNA. After 8 h the cells were
527 harvested, lysed by phenol, and total tRNA isolated using a series of differential precipitation
528 steps (60). Approximately half of the recovered tRNA was a substrate for charging by MetRS.
529 The charging reaction (2 mL) contained approximately 200 nmoles of total tRNA and 10 nmoles
530 of MetRS in the presence of 1 mM methionine, 2 mM ATP, 10 mM $MgCl_2$, 20 mM KCl, 4 mM
531 DTT, 50 μg/mL BSA, and 50 mM Tris-HCl pH 7.5. After 10 min at 37 °C a 4.0 μL aliquot of the
532 reaction was removed for determination of the charging efficiency as described by Gamper et *al*
533 (61). The remaining reaction was incubated for 10 min at 37 °C with 1.7 μmoles of 10-
534 formyltetrahydrofolate and 20 nmoles of methionyl formyl transferase to convert Met-tRNA$_i^{Met}$ to
535 fMet-tRNA$_i^{Met}$. The reaction was quenched by adding a 0.1 volume of 2.5 M NaOAc pH 5.0.
536 Following an equal volume pH 5 phenol-chloroform-isoamyl alcohol extraction (80:17:3), the
537 tRNA was ethanol precipitated, dissolved in 300 μL 25 mM NaOAc pH 5.0, and stored at -70 °C.
538 Approximately 200 nmoles of tRNA was recovered, of which 45% was fMet-tRNA$_i^{Met}$.

539 *Reconstitution of Rsh-bound 70S initiation complex: 70S* ribosomes prepared from a low-zinc
540 culture of isogenic Δ*rsh*/Δ*mpy*/Δ*mrf* triple mutant of *M. smegmatis* were dialyzed at 4°C with low-
541 magnesium buffer (20 mM HEPES-K pH7.5, 30 mM NH_4Cl, 0.5 mM $MgCl_2$, 5 mM β-
542 mercaptoethanol) to dissociate the 30S and 50S subunits. Two rounds of dialysis were
543 performed, with fresh buffer change every four hours. Subunit dissociation was confirmed by
544 loading 2.4 picomoles of the dialyzed ribosomes onto a 10-40% sucrose density gradient.
545 Another 2.4 pmoles of dissociated ribosomes were mixed with five-fold molar excess of fMet-
546 $tRNA_i^{fMet}$, a synthetic mRNA template (GGCAAGGAGGUAAAAAUGUUCAAAAAA-Flour) (IDT,
547 USA), recombinant His_6-IF2, recombinant His_6-Rsh, and either GTP or GMP-PNP (Sigma-
548 Aldrich) in a 100 µL reaction in buffer I (20 mM HEPES-K pH 7.5, 30 mM NH_4Cl, 1 mM $MgCl_2$, 5
549 mM β-mercaptoethanol), and the mixture was incubated at 37 °C for 15 minutes to allow
550 formation of the initiation complex on the 30S subunit. Then 25 µL of buffer II (20 mM HEPES-K
551 pH7.5, 30 mM NH4Cl, 50 mM MgCl2, 5 mM β-mercaptoethanol, 600mM KCl) was added to the
552 mixture, thereby bringing the final concentration of $MgCl_2$ and KCl to 10mM and 120 mM,
553 respectively. The reaction was then incubated for an additional 30 minutes at 37°C to allow
554 joining of the 50S subunit. Resulting complexes were either used for structural analysis or
555 resolved on a 15 mL 10-40% sucrose density gradient centrifuged at 35000 rpm for 135 minutes
556 using SW41 rotor on an Optima L-90K ultracentrifuge (Beckman Coulter), and the resolved
557 particles were fractionated as previously described (59). For immunoblotting analysis, content of
558 the indicated fractions were precipitated using Methanol-chloroform extraction as previously
559 described (39). Briefly, each fraction was vortexed with 4X volume of methanol for 5-10 seconds
560 and centrifuged for 10 seconds at 13,200 rpm on a benchtop centrifuge before adding one
561 volume of chloroform. The mixture was further centrifuged at 13,200 rpm for 60 seconds, after
562 which 3X volume of water was added and the mixture was vortexed before further centrifugation
563 at 13,200 rpm for 60 seconds. The upper aqueous layer was discarded while retaining the
564 interface and the organic layer, which was mixed with 3X volume of methanol, vortexed and

565 centrifuged at 13,200 rpm for 2 minutes. The supernatant was discarded, and the resulting
566 pellet was dried and resuspended in 0.1 M Tris containing 8M urea for further analysis of
567 proteins by immunoblotting.
568
569
570 **Immunoblotting**
571 Total cell lysates (10 µg) or purified 70S ribosomes (2.4 pmoles) were used for detecting S13,
572 MPY, Mrf-FLAG, and $S14_{C-}$, while 24 pmoles ribosome were used for detecting Rsh. Samples
573 were resolved on 8% SDS-PAGE (for FLAG, Rsh and GroEL analysis) or 12% SDS-PAGE (for
574 MPY, $S14_{C-}$ and S13), and proteins were probed with anti-FLAG (1:5000, Genescript), anti-GroEL
575 (1:5000, Enzo), anti-RelA (1:5000), anti-S13 of *E. coli* (1:100, The Developmental Studies
576 Hybridoma Bank), endogenously raised anti-MPY (1:5000) and anti-$S14_{C-}$ (1:2000) antibodies.
577
578 **ppGpp extraction and analysis**
579 Cells of specified *M. smegmatis* strains were grown in Sauton's medium with either 1 mM Zn or
580 1 µM TPEN for 96 hours, after which 1 mL of the culture was labelled with 100 □Ci/mL of ^{32}P
581 KH_2PO_4 (Perkin Elmer, 900-1100mCi/mmol) for 6 hours on a shaker at 37 ºC. Labeled cells were
582 washed once with TBST (20mM Tris pH7.6 + 150 mM NaCl + 0.05% Tween 80). Half of the cells
583 (0.5 mL) were pelleted and resuspended in 25 µL of 4M formic acid and kept frozen at -20 ºC until
584 ready for extraction. Remaining 0.5 mL cells were starved for 3 hours in TBST, or metal-chelated
585 TBST, or zinc-supplemented TBST as specified. Following treatment, both pre- and post-starved
586 cells were pelleted and resuspended in 25 □L of 4M formic acid and incubated on ice for 10
587 minutes. Cell suspensions were frozen on dry ice for 10 minutes and thawed at 37 ºC for 10
588 minutes. The freeze-thaw cycle was repeated 5 times, after which the cell lysates were
589 centrifuged at 13,500 rpm for 5 minutes at 4 ºC, and 5 □L of the supernatants containing ^{32}P
590 labeled intracellular nucleotides were resolved on a 20 x 20 cm plastic PEI cellulose F TLC plate

591 (Millipore) using 1.5 M KH_2PO_4 pH 3.4 as a solvent. When the solvent front reached the top of the
592 plate, the plate was dried and exposed to X-ray film. 5 □L of 100 mM nonradioactive nucleotides
593 [ppGpp (Trilink), ATP, GDP and GTP (Thermo Fisher)] were also resolved as positional markers,
594 which were visualized by handheld UV lamp (Stuart, Cole Palmer). For quantitative analysis, pixel
595 density of ppGpp spot were determined from densitometric scan of radiographs using Fiji
596 (ImageJ). Using the counts from low-zinc culture of wild-type strain in a radiograph as the common
597 denominator, relative counts in other samples from the same radiograph were calculated.
598
599 **Cryo-electron microscopy and image processing** Quantifoil
600 holey carbon copper grids R 1.2/1.3 were coated with a continuous layer of carbon (~50 Å
601 thick). After glow discharge for 30 s on a plasma sterilizer, 4 µl of the 200 nM Rsh-bound pre-
602 elongation complex sample was placed on the grids. The sample was incubated on the grids for
603 15 s at 4 °C and 100% humidity, followed by blotting for 4 s before flash-freezing into the liquid
604 ethane using a Vitrobot IV (FEI). Data were collected on a Titan Krios electron microscope at
605 300 keV using a K3 direct electron-detecting camera (Gatan). −1.50 to −2.50 µm defocus range
606 was used at a magnification of 81,000×, yielding a pixel size of 0.846 Å. The dose rate of 23.3
607 electrons/pixel/second with a 2.05 second exposure time, with 41 frames of 0.05 second
608 duration each, resulted in a total dose of 66.59 e/Å−2. RELION 4.0 was used for data
609 processing. Image stacks were gain-corrected, dose-weighted, and aligned using MotionCor2
610 (62) for 9,103 micrographs. The contrast transfer function of each aligned micrograph was
611 estimated using CTFFIND-4.1 (63). A subset of micrographs was used for particle picking
612 followed by 2D classification. Relevant 2D classes were used for reference-based particle
613 picking on all micrographs yielding 1,928,609 particles. These particles were 2D classified and
614 suitable class averages selected (389,456 particles) (Fig. S7). The selected particles were 3D
615 refined and followed by 3D classification. Classes corresponding to monosomes with 349,437
616 particles were selected for further processing. In order to resolve structural heterogeneity in the

617 monosome particles, we performed 3D refinement using a large subunit mask followed by three
618 rounds of fixed orientation 3D classification. In the first round of fixed orientation 3D
619 classification, we used an SSU mask to resolve the SSU conformations into six classes. Class I
620 with 158,489 particles showed density corresponding to P-site tRNA and Rsh, representing the
621 Rsh-bound pre-elongation complex. We then performed the second round of fixed orientation
622 3D classification on this class using a mask encompassing the entire inter-ribosomal subunit
623 space such as the L7/L12-stalk, A-, P-, and E-site tRNA binding sites, and the L1-stalk regions.
624 The second round of fixed orientation 3D classification resolved the conformational and
625 particularly compositional heterogeneity in the masked region. We derived four classes with P-
626 site tRNA density and two classes with P-site tRNA and Rsh densities. We performed the third
627 round of fixed orientation 3D classification combining the two classes with P-site tRNA and Rsh
628 densities, (49,058 particles) using a mask encompassing the P-site tRNA and Rsh. Two of the
629 classes, one with 16,013 particle and another with 20,308 particles, showed densities
630 corresponding to P-site tRNA and ZBD and ACT domains of Rsh. However, density
631 corresponding to ACT domain was slightly better in the class with 16,013 particles and was
632 refined to a global resolution of 2.98 Å and was used to model the Rsh-ACT domain. Since the
633 densities corresponding to ZBD were very similar in both classes, they were merged. The
634 combined class with a total of 36,321 particles showed significant density corresponding to P-
635 site tRNA and Rsh-ZBD. CTF refinement and Bayesian polishing of the combined class with a
636 total of 36,321 particles yielded a map with a global resolution of 2.7 Å and was used to model
637 the Rsh-ZBD.

638 **Model building** Coordinates
639 of the large and small subunits from our published C- *M. smegmatis* ribosome structure
640 (PDB:6DZI) were docked as rigid bodies into the cryo-EM map using Chimera 1.14 (64). To
641 achieve optimal fitting, we adjusted the model based on the densities in Coot (65). The model
642 was subsequently refined using PHENIX 1.14 (66). A predicted structure of *M. smegmatis* Rsh

643 is available in the Alphafold Protein Structure database (67). This structure was docked into the
644 corresponding density in the cryo-EM map using Chimera 1.14 (64) and subsequently refined
645 with Coot (65) and PHENIX 1.14 (66). A validation report for the model was obtained from
646 PHENIX 1.14 (66). The overall statistics of EM reconstruction and molecular modeling are listed
647 in Table S3. ChimeraX-1.0 (68) and Chimera 1.14 (64) were used to generate the structural
648 figures in the manuscript.
649

Acknowledgments:

This work was supported by grants to AKO (NIH: AI132422, NIH: AI163599), CS (AI111696), RKA (NIH:GM61576), and YMH (NIH: GM134931). R.K.A. also acknowledges support to his lab through NIH R01 grants AI132422, GM139277 and AI155473. Support from the Wadsworth Center core facilities–Applied Genomic Technologies and the media core facility– is acknowledged. We also acknowledge Wadsworth Center's and New York Structural Biology Center's (NYSBC's) 3D-EM facilities. NYSBC EM facilities are supported by grants from the Simons Foundation (349247), NYSTAR, the NIH (GM103310) and the Agouron Institute (F00316). Authors acknowledge technical support from Kelley-Hurst, and discussions with Drs. Pallavi Ghosh, Keith Derbyshire, Todd Gray and Erica Lasek-Nesselquist.

Authors' Contribution:

YL, RT, JC and AKO designed and performed genetics and biochemical experiments; SM, MRS, SRM, NKB and RKA designed and performed structural analysis and model construction; JP, CS, HG and YMH provided reagents. All authors wrote the manuscript.

Financial Conflict of Interest:

Authors declare no financial conflict of interest.

Data Deposition:

The cryo-EM map and atomic coordinates of the *M. smegmatis* 70S-Rsh-fMet-tRNAiMet complex are deposited in the Electron Microscopy and PDB Data Bank (wwPDB.org). Accession codes are EMD-29397 and 8FR8 respectively.

672 **References**

673 1. M. Cashel, J. Gallant, Two compounds implicated in the function of the RC gene of
674 Escherichia coli. *Nature* **221**, 838-841 (1969).
675 2. D. Chatterji, A. K. Ojha, Revisiting the stringent response, ppGpp and starvation signaling.
676 *Curr Opin Microbiol* **4**, 160-165 (2001).
677 3. K. Potrykus, M. Cashel, (p)ppGpp: still magical? *Annu Rev Microbiol* **62**, 35-51 (2008).
678 4. J. Prusa, D. X. Zhu, C. L. Stallings, The stringent response and Mycobacterium tuberculosis
679 pathogenesis. *Pathog Dis* **76** (2018).
680 5. J. L. Dahl *et al.*, The role of RelMtb-mediated adaptation to stationary phase in long-term
681 persistence of Mycobacterium tuberculosis in mice. *Proc Natl Acad Sci U S A* **100**, 10026-
682 10031 (2003).
683 6. C. L. Stallings *et al.*, CarD is an essential regulator of rRNA transcription required for
684 Mycobacterium tuberculosis persistence. *Cell* **138**, 146-159 (2009).
685 7. L. A. Weiss, C. L. Stallings, Essential roles for Mycobacterium tuberculosis Rel beyond the
686 production of (p)ppGpp. *J Bacteriol* **195**, 5629-5638 (2013).
687 8. J. P. Richards, W. Cai, N. A. Zill, W. Zhang, A. K. Ojha, Adaptation of Mycobacterium
688 tuberculosis to Biofilm Growth Is Genetically Linked to Drug Tolerance. *Antimicrob Agents*
689 *Chemother* **63** (2019).
690 9. C. Vilcheze, W. R. Jacobs, Jr., The Isoniazid Paradigm of Killing, Resistance, and Persistence
691 in Mycobacterium tuberculosis. *J Mol Biol* **431**, 3450-3461 (2019).
692 10. N. K. Dutta *et al.*, Inhibiting the stringent response blocks Mycobacterium tuberculosis
693 entry into quiescence and reduces persistence. *Sci Adv* **5**, eaav2104 (2019).
694 11. W. Ross, C. E. Vrentas, P. Sanchez-Vazquez, T. Gaal, R. L. Gourse, The magic spot: a ppGpp
695 binding site on E. coli RNA polymerase responsible for regulation of transcription
696 initiation. *Mol Cell* **50**, 420-429 (2013).
697 12. Z. D. Dalebroux, M. S. Swanson, ppGpp: magic beyond RNA polymerase. *Nat Rev Microbiol*
698 **10**, 203-212 (2012).
699 13. S. Diez, J. Ryu, K. Caban, R. L. Gonzalez, Jr., J. Dworkin, The alarmones (p)ppGpp directly
700 regulate translation initiation during entry into quiescence. *Proc Natl Acad Sci U S A* **117**,
701 15565-15572 (2020).
702 14. S. E. Irving, N. R. Choudhury, R. M. Corrigan, The stringent response and physiological
703 roles of (pp)pGpp in bacteria. *Nat Rev Microbiol* **19**, 256-271 (2021).
704 15. G. C. Atkinson, T. Tenson, V. Hauryliuk, The RelA/SpoT homolog (RSH) superfamily:
705 distribution and functional evolution of ppGpp synthetases and hydrolases across the tree
706 of life. *PLoS One* **6**, e23479 (2011).
707 16. T. Hogg, U. Mechold, H. Malke, M. Cashel, R. Hilgenfeld, Conformational antagonism
708 between opposing active sites in a bifunctional RelA/SpoT homolog modulates (p)ppGpp
709 metabolism during the stringent response [corrected]. *Cell* **117**, 57-68 (2004).
710 17. A. Brown, I. S. Fernandez, Y. Gordiyenko, V. Ramakrishnan, Ribosome-dependent
711 activation of stringent control. *Nature* **534**, 277-280 (2016).
712 18. A. B. Loveland *et al.*, Ribosome*RelA structures reveal the mechanism of stringent
713 response activation. *Elife* **5** (2016).

714 19. S. Arenz *et al.*, The stringent factor RelA adopts an open conformation on the ribosome
715 to stimulate ppGpp synthesis. *Nucleic Acids Res* **44**, 6471-6481 (2016).
716 20. P. Pausch *et al.*, Structural Basis for Regulation of the Opposing (p)ppGpp Synthetase and
717 Hydrolase within the Stringent Response Orchestrator Rel. *Cell Rep* **32**, 108157 (2020).
718 21. T. M. Wendrich, G. Blaha, D. N. Wilson, M. A. Marahiel, K. H. Nierhaus, Dissection of the
719 mechanism for the stringent factor RelA. *Mol Cell* **10**, 779-788 (2002).
720 22. K. S. Winther, M. Roghanian, K. Gerdes, Activation of the Stringent Response by Loading
721 of RelA-tRNA Complexes at the Ribosomal A-Site. *Mol Cell* **70**, 95-105 e104 (2018).
722 23. H. Takada *et al.*, Ribosome association primes the stringent factor Rel for tRNA-dependent
723 locking in the A-site and activation of (p)ppGpp synthesis. *Nucleic Acids Res* **49**, 444-457
724 (2021).
725 24. M. Gropp, Y. Strausz, M. Gross, G. Glaser, Regulation of Escherichia coli RelA requires
726 oligomerization of the C-terminal domain. *J Bacteriol* **183**, 570-579 (2001).
727 25. A. Avarbock *et al.*, Functional regulation of the opposing (p)ppGpp synthetase/hydrolase
728 activities of RelMtb from Mycobacterium tuberculosis. *Biochemistry* **44**, 9913-9923
729 (2005).
730 26. V. Jain, R. Saleem-Batcha, A. China, D. Chatterji, Molecular dissection of the mycobacterial
731 stringent response protein Rel. *Protein Sci* **15**, 1449-1464 (2006).
732 27. H. Takada *et al.*, The C-Terminal RRM/ACT Domain Is Crucial for Fine-Tuning the Activation
733 of 'Long' RelA-SpoT Homolog Enzymes by Ribosomal Complexes. *Front Microbiol* **11**, 277
734 (2020).
735 28. H. Tamman *et al.*, A nucleotide-switch mechanism mediates opposing catalytic activities
736 of Rel enzymes. *Nat Chem Biol* **16**, 834-840 (2020).
737 29. K. J. Turnbull, I. Dzhygyr, S. Lindemose, V. Hauryliuk, M. Roghanian, Intramolecular
738 Interactions Dominate the Autoregulation of Escherichia coli Stringent Factor RelA. *Front*
739 *Microbiol* **10**, 1966 (2019).
740 30. U. Mechold, H. Murphy, L. Brown, M. Cashel, Intramolecular regulation of the opposing
741 (p)ppGpp catalytic activities of Rel(Seq), the Rel/Spo enzyme from Streptococcus
742 equisimilis. *J Bacteriol* **184**, 2878-2888 (2002).
743 31. S. Ronneau *et al.*, Regulation of (p)ppGpp hydrolysis by a conserved archetypal regulatory
744 domain. *Nucleic Acids Res* **47**, 843-854 (2019).
745 32. F. L. Gratani *et al.*, Regulation of the opposing (p)ppGpp synthetase and hydrolase
746 activities in a bifunctional RelA/SpoT homologue from Staphylococcus aureus. *PLoS Genet*
747 **14**, e1007514 (2018).
748 33. B. P. English *et al.*, Single-molecule investigations of the stringent response machinery in
749 living bacterial cells. *Proc Natl Acad Sci U S A* **108**, E365-373 (2011).
750 34. D. Avarbock, J. Salem, L. S. Li, Z. M. Wang, H. Rubin, Cloning and characterization of a
751 bifunctional RelA/SpoT homologue from Mycobacterium tuberculosis. *Gene* **233**, 261-269
752 (1999).
753 35. T. P. Primm *et al.*, The stringent response of Mycobacterium tuberculosis is required for
754 long-term survival. *J Bacteriol* **182**, 4889-4898 (2000).
755 36. A. K. Ojha, T. K. Mukherjee, D. Chatterji, High intracellular level of guanosine
756 tetraphosphate in Mycobacterium smegmatis changes the morphology of the bacterium.
757 *Infect Immun* **68**, 4084-4091 (2000).

758 37. D. Avarbock, A. Avarbock, H. Rubin, Differential regulation of opposing RelMtb activities
759 by the aminoacylation state of a tRNA.ribosome.mRNA.RelMtb complex. *Biochemistry* **39**,
760 11640-11648 (2000).
761 38. Y. Li *et al.*, Zinc depletion induces ribosome hibernation in mycobacteria. *Proc Natl Acad*
762 *Sci U S A* **115**, 8191-8196 (2018).
763 39. Y. Li, J. H. Corro, C. D. Palmer, A. K. Ojha, Progression from remodeling to hibernation of
764 ribosomes in zinc-starved mycobacteria. *Proc Natl Acad Sci U S A* **117**, 19528-19537
765 (2020).
766 40. S. Prisic *et al.*, Zinc regulates a switch between primary and alternative S18 ribosomal
767 proteins in Mycobacterium tuberculosis. *Mol Microbiol* **97**, 263-280 (2015).
768 41. K. Izutsu, A. Wada, C. Wada, Expression of ribosome modulation factor (RMF) in
769 Escherichia coli requires ppGpp. *Genes Cells* **6**, 665-676 (2001).
770 42. R. D. Hood, S. A. Higgins, A. Flamholz, R. J. Nichols, D. F. Savage, The stringent response
771 regulates adaptation to darkness in the cyanobacterium Synechococcus elongatus. *Proc*
772 *Natl Acad Sci U S A* **113**, E4867-4876 (2016).
773 43. H. Schafer *et al.*, The alarmones (p)ppGpp are part of the heat shock response of Bacillus
774 subtilis. *PLoS Genet* **16**, e1008275 (2020).
775 44. X. Gao, J. Yeom, E. A. Groisman, The expanded specificity and physiological role of a
776 widespread N-degron recognin. *Proc Natl Acad Sci U S A* **116**, 18629-18637 (2019).
777 45. P. Kudrin *et al.*, The ribosomal A-site finger is crucial for binding and activation of the
778 stringent factor RelA. *Nucleic Acids Res* **46**, 1973-1983 (2018).
779 46. T. Sprink *et al.*, Structures of ribosome-bound initiation factor 2 reveal the mechanism of
780 subunit association. *Sci Adv* **2**, e1501502 (2016).
781 47. R. A. Marshall, C. E. Aitken, J. D. Puglisi, GTP hydrolysis by IF2 guides progression of the
782 ribosome into elongation. *Mol Cell* **35**, 37-47 (2009).
783 48. P. P. Datta, M. R. Sharma, L. Qi, J. Frank, R. K. Agrawal, Interaction of the G ' domain of
784 elongation factor G and the C-terminal domain of ribosomal protein L7/L12 during
785 translocation as revealed by cryo-EM. *Molecular Cell* **20**, 723-731 (2005).
786 49. T. Yokoyama *et al.*, Structural insights into initial and intermediate steps of the ribosome-
787 recycling process. *Embo J* **31**, 1836-1846 (2012).
788 50. J. D. Friesen, N. P. Fiil, J. M. Parker, W. A. Haseltine, A new relaxed mutant of Escherichia
789 coli with an altered 50S ribosomal subunit. *Proc Natl Acad Sci U S A* **71**, 3465-3469 (1974).
790 51. J. Parker, R. J. Watson, J. D. Friesen, A relaxed mutant with an altered ribosomal protein
791 L11. *Mol Gen Genet* **144**, 111-114 (1976).
792 52. X. Yang, E. E. Ishiguro, Involvement of the N terminus of ribosomal protein L11 in
793 regulation of the RelA protein of Escherichia coli. *J Bacteriol* **183**, 6532-6537 (2001).
794 53. I. S. Gabashvili *et al.*, Solution structure of the E. coli 70S ribosome at 11.5 A resolution.
795 *Cell* **100**, 537-549 (2000).
796 54. H. Gao *et al.*, Study of the structural dynamics of the E coli 70S ribosome using real-space
797 refinement. *Cell* **113**, 789-801 (2003).
798 55. D. Pletzer *et al.*, The Stringent Stress Response Controls Proteases and Global Regulators
799 under Optimal Growth Conditions in Pseudomonas aeruginosa. *mSystems* **5** (2020).
800 56. C. Andreini, L. Banci, I. Bertini, A. Rosato, Zinc through the three domains of life. *J*
801 *Proteome Res* **5**, 3173-3178 (2006).

57. R. Sankaranarayanan *et al.*, The structure of threonyl-tRNA synthetase-tRNA(Thr) complex enlightens its repressor activity and reveals an essential zinc ion in the active site. *Cell* **97**, 371-381 (1999).
58. J. A. Judd *et al.*, A Mycobacterial Systems Resource for the Research Community. *mBio* **12** (2021).
59. Y. Li *et al.*, Purification of Hibernating and Active C- Ribosomes from Zinc-Starved Mycobacteria. *Methods Mol Biol* **2314**, 151-166 (2021).
60. v. Ehrenstein, Isolation of sRNA from intact Escherichia coli cells. *Methods in Enzymology* **12A**, 588-596 (1967).
61. H. Gamper, Y. M. Hou, A Label-Free Assay for Aminoacylation of tRNA. *Genes (Basel)* **11** (2020).
62. S. Q. Zheng *et al.*, MotionCor2: anisotropic correction of beam-induced motion for improved cryo-electron microscopy. *Nat Methods* **14**, 331-332 (2017).
63. A. Rohou, N. Grigorieff, CTFFIND4: Fast and accurate defocus estimation from electron micrographs. *J Struct Biol* **192**, 216-221 (2015).
64. E. F. Pettersen *et al.*, UCSF Chimera--a visualization system for exploratory research and analysis. *J Comput Chem* **25**, 1605-1612 (2004).
65. P. Emsley, B. Lohkamp, W. G. Scott, K. Cowtan, Features and development of Coot. *Acta Crystallogr D Biol Crystallogr* **66**, 486-501 (2010).
66. P. D. Adams *et al.*, PHENIX: a comprehensive Python-based system for macromolecular structure solution. *Acta Crystallogr D Biol Crystallogr* **66**, 213-221 (2010).
67. J. Jumper *et al.*, Highly accurate protein structure prediction with AlphaFold. *Nature* **596**, 583-589 (2021).
68. E. F. Pettersen *et al.*, UCSF ChimeraX: Structure visualization for researchers, educators, and developers. *Protein Sci* **30**, 70-82 (2021).

829 **Figure legends:**
830
831 **Figure 1: Attenuated stringent response and loss of Rsh in zinc-starved mycobacteria. A.**
832 A conserved domain architecture in mycobacterial RelA/SpoT homologue (Rsh) compared to
833 RelA nd Rel in other species. The N-terminal domain (NTD) containing the hydrolase (HYD) and
834 synthase (SYN) is distinguished from the C-terminal domain (CTD) by TGS (Thr-RS, GTPase and
835 SpoT) and alpha-helix domain (AHD). The CTD is comprised of ZBD (zinc binding domain) and
836 ACT (aspartokinase, chorismate mutase and TyrA) subdomains. **B.** Radio-TLC showing ppGpp
837 levels in cultures of wild-type (WT) *M. smegmatis* isolated from high-zinc (1mM $ZnSO_4$) and low-
838 zinc (1 μM TPEN) Sauton's medium after 96 hours of growth. ^{32}P-labeled sodium phosphate (100
839 μCi/mL) was added to the cultures six hours prior to starvation in TBST for three hours. After
840 starvation nucleotides were extracted in formic acid and amounts equivalent to 50000 cpm were
841 analyzed by TLC. Purified cold ppGpp was loaded as positional marker. The plot shows ppGpp
842 levels in high-zinc WT samples relative to their low-zinc counterparts from four biologically
843 independent experiments. **C.** Radio-TLC showing ppGpp levels in WT cells cultured for 96-hours
844 in high-zinc Sauton's medium, then labelled for six hours, and resuspended in either TBST, or
845 Chelex 100-treated TBST ($TBST_{ch}$), or zinc-supplemented $TBST_{ch}$ ($TBST_{Zn}$). A Δ*rsh* mutant was
846 used as control in panels B and C. **D**. Immunoblot analysis of Rsh levels in 70S ribosomes purified
847 from 96-hour-old high-and low-zinc cultures of *M. smegmatis* strains described in panel B. S14c-
848 was used as a marker for the remodeled C- ribosome, while S13 was used as the loading control
849 for ribosomes. In the set of immunoblots on the right, cell lysates from the samples used for
850 ribosome analysis were probed. The asterisk indicates a non-specific unknown protein cross-
851 reactive to Rsh antibody. The plots to the extreme right show the normalized average difference
852 in Rsh between high- and low-zinc cultures from three independent experiments.
853
854 **Figure 2: Mrf accumulation causes loss of Rsh. A-B.** Analysis of Rsh in 70S ribosomes (A)
855 and cell lysates (B) from high- or low-zinc cultures of Δ*mrf* and complemented (Δ*mrf*comp) strains

856 of *M. smegmatis.* High and low-zinc cultures of WT were controls. $S14_{c-}$, S13 and GroEL were
857 probed as loading controls for ribosomes or cell lysates as indicated. The asterisk in panel B
858 indicates a non-specific protein cross-reactive to Rsh antibody. **C.** Radio-TLC showing ppGpp
859 levels in 96-hour old high- or low-zinc cultures of WT and low-zinc cultures of Δ*mrf and* Δ*mrfcomp*
860 of *M. smegmatis* strains after 3-hours of starvation in TBST. Purified cold ppGpp was loaded as
861 positional marker. The plot shows relative ppGpp levels in each sample compared to the level in
862 low-zinc culture of WT from two biologically independent experiments. **D.** Ectopic Mrf expression
863 causes loss of Rsh. Levels of Rsh in the cell lysates of a *M. smegmatis* strain (pYL222) expressing
864 FLAG-tagged Mrf* under the acetamide-inducible promoter. Cells were cultured in high-zinc
865 Sauton's medium (1mM ZnSO4) containing 0.2% succinate as the carbon source until OD 0.6,
866 after which Mrf* expression was induced with 0.2% acetamide, and cells were grown for 96 hours
867 from inoculation. Uninduced cells were used as the reference. As controls, 96-hour old cells from
868 the wildtype (WT) and Δ*rsh* strains cultured in either high- or low-zinc (1μM TPEN) Sauton's
869 medium with succinate as the carbon source. The plot shows average normalized density of Rsh
870 from two independent experiments. **E.** Analysis of Rsh in ribosomes purified from 96-hour-old
871 induced or uninduced high-zinc cultures of pYL222 strain. **F.** Simultaneous accumulation of Rsh
872 and Mrf in YL9 cells (Li et al. 2020) upon conditional depletion of ClpP1 protease. Cells were
873 grown in high-zinc Sauton's medium until OD of 0.6, after which anhydrotetracycline (ATc) was
874 added to induce CRISPRi system to deplete ClpP1. Cell lysates were analyzed after 16 hours of
875 ClpP1 depletion. A parallel uninduced cells were used as control. YL9 cells grown for 96 hours in
876 high- or low-zinc Sauton's medium without ATc were used as controll. The plot shows average
877 normalized density of Rsh from two independent experiments.
878
879 **Figure 3**: **Ribosome binding residues in Rsh are critical for its intracellular stability**. **A.** (Top)
880 Sequence alignment of the C- terminal region of Rsh from *E. coli*, *M. smegmatis* and *M.*
881 *tuberculosis* depicting the CCHC like zinc-finger (highlighted yellow) in the ZBD. (Bottom)

882 Superimposition of the structure (PDBID: 5IQR) of the ZBD region from *E. coli* (yellow) and *M.*
883 *smegmatis* (red). Zinc atom coordinated (shown with dashed lines) by the CCHC motif (shown as
884 ball-and-stick model and numbered based on *E. coli* sequence) has been zoomed in the image
885 to the right. The corresponding residues from *M. smegmatis* (shown in red ball-and-stick model)
886 predict similarity in spatial orientation with respect to their *E. coli* counterparts. **B.** Immunoblot
887 analysis of Rsh variants ($C_{666}G$, $D_{691}R$ and $C_{692}F$) in cell lysates and 70S ribosomes purified from
888 96-hour-old high-zinc cultures of a Δ*rsh* strain *of M. smegmatis* expressing each Rsh variant
889 individually from an integrative plasmid (pYL238, pYL240, pYL241, pYL242 for Rsh, Rsh_{C666G},
890 Rsh_{D691R} and Rsh_{C692F}, respectively). Cultures of Δ*rsh* strain expressing WT Rsh were controls.
891 Normalized average levels of Rsh and its variants in cell lysates from three independent
892 experiments are shown in the plot. **C.** *In vitro* ribosome binding of recombinant Rsh and its
893 variants. 2.4 picomoles of 70S ribosomes purified from a 96-hour old high-zinc culture of Δ*rsh*
894 strain of *M. smegmatis* were mixed with 1.2 picomoles of Rsh or variant proteins (purified from
895 recombinant *E. coli* harboring pYL243, pYL246, pYL247, pY248 for Rsh, Rsh_{C666F}, Rsh_{D691R} and
896 Rsh_{C692F}, respectively) and the mixture was incubated for 30 minutes at 37 ◦C. The complex was
897 separated by ultracentrifugation through a 32% sucrose cushion. S13 was probed as the loading
898 control. The plot shows quantitative analysis of Rsh from two biologically independent
899 experiments.
900
901 **Figure 4**: **Rsh interaction with a 70S translation initiation complex. A.** Co-sedimentation of
902 Rsh with the 50S ribosomal subunit. Pellets resulting from ultracentrifugation on a 32% sucrose
903 cushion were analyzed for S13 to confirm SSU, $L33_{C-}$ to confirm LSU, and Rsh to test preferential
904 subunit binding. Rsh in the absence of ribosomes was included as control to rule out
905 sedimentation of free protein. Purified Rsh was loaded as marker. **B-C.** Reconstitution of Rsh-
906 bound pre-elongation complex in the presence of GTP (B) or GMP-PNP (C). Dissociated
907 ribosomes (Figure S6) were mixed with indicated ligands in the presence of GTP or GMP-PNP.

908 After incubation for 15 minutes in low-magnesium (1mM $MgCl_2$) buffer, recombinant Rsh was
909 added, and magnesium was adjusted to 10 mM. The resulting mixture was incubated for
910 additional 30 minutes. The complex was resolved in 10-40% SDG, and fractions corresponding
911 to the 70S-peak and its margin were analyzed for Rsh, IF2 and indicated ribosomal proteins by
912 immunoblotting using anti-Rsh, anti-His_6 (for IF2), anti-S13 and anti-L31 antibodies. All reagents
913 in the reactions in panels B and C were added in 5-fold molar excess relative to the ribosomal
914 subunits. **D.** 2.7 Å resolution cryo-EM structure of the 70S-Rsh complex in late initiation state of
915 translation, with a fMet-$tRNA_i^{Met}$ present in the P-site (green), mRNA (brown), and two C-terminal
916 domains of Rsh, ZBD (magenta) and ACT (blue). The 30S and 50S subunits are shown in yellow
917 and blue, respectively. **E**. Ribosomal components interacting with Rsh ZBD and ACT domain,
918 along with the fMet-$tRNA_f^{Met}$ in the P-site (green), are shown. ZBD interacts with components of
919 inter-subunit bridge B1a, uS19 (light green), and the A-site finger (ASF, sky blue). ACT interacts
920 with the 50S components uL16 (sky blue), L11, and 23S rRNA helices H43/44 (sky blue). F.
921 Superimposition of *M. smegmatis* 70S-Rsh, *E. coli* 70S-RelA (PDB ID: 5KPV) and *E. coli* 70S-IF2
922 (PDB ID: 6HTQ) structures, comparing their binding sites and conformations on the ribosome.
923 Position of IF2 (VI-C1, cyan) suggests a direct steric clash (highlighted by red dotted circle) with
924 the *E. coli* RelA's α-helical domain (RelA-AHD, light coral). *M. smegmatis* Rsh-ACT (Ms- ACT,
925 blue) is rotated by ~14° (indicated by a red arrow) relative to the *E. coli* RelA-ACT (Ec-ACT, light
926 blue), while the ZBD domains (Ms-ZBD, magenta and Ec-ZBD in light purple) have the same
927 position.
928
929 **Figure 5: The Rsh-ACT domain interacts with the L7/L12 stalk base. A.** Superimposition of
930 the Rsh/Rel A interacting components from the 70S-Rsh/RelA complex structures from *M.*
931 *smegmatis* (Ms) 70S-Rsh (ZBD, magenta; ACT, blue), *B. subtilis* (Bs) 70S-Rsh (ZBD, light pink;
932 ACT, gray), and *E. coli* (Ec) 70S-RelA (ZBD, light purple; ACT, steel blue). Only components
933 interacting with RelA/Rsh, L7/L12 stalk base (H43/H44 in blue), A-site finger (ASF in blue) uL16

934 and uL11 (light pink), the A/R tRNA (light coral) and uS19 (sea green), along with the P-site tRNA
935 (light gray), are displayed. **B.** Superimposition of the C-terminal ZBD and ACT domain from Ms,
936 Bs, and Ec (color-coded as in panel A) highlighting the rotation in Ms-ACT domain with respect
937 to Ms-ZBD. **C.** Interactions of Ms Rsh-ACT (blue) with L11 (light pink) and the 23S rRNA helices
938 H43/44 (light blue) are shown from two viewing directions.
939
940 **Figure 6: Structural basis of Rsh exclusion from a Mpy-bound 70S ribosome. A**.
941 Superimposition of Ms 70S-Mpy (gray, PDB ID:6DZI) and Ms 70S-Rsh (gold) structures. Rsh
942 (ZBD, magenta; ACT, blue) and Mpy (green) are shown in the space-filled rendering. **B**. The 16S
943 rRNAs corresponding to head domain of the 30S subunit in panel A has been enlarged to highlight
944 their relative position in the two functional states. **C**. The position of uS19 (gray) in the Mpy-bound
945 state would disrupt the observed interactions between Rsh-ZBD (magenta) and uS19 (orange).
946
947 **Figure 7**: **Model of a dynamic interaction of Rsh with the ribosome in mycobacteria,**
948 **influenced by three distinct conditions**. In a nutrient-rich condition supporting high translation
949 activity, labile Rsh predominantly remains associated with the free 50S subunit, which confers
950 stability to the protein. Rsh-50S complex joins with a 30S pre-initiation complex (pre-IC). Following
951 the release of initiation factors, Rsh likely remains in the pre-elongation intermediate (PEI), which
952 in an unrotated conformation is ready to elongate upon entry of the first A- site tRNA (step A).
953 Rsh is likely sterically displaced during inter-subunit rotation associated with the first cycle of
954 elongation (step B). Free Rsh associates with 50S subunit (step C) and the cycle continues until
955 a deacylated tRNA enters the A-site at the second codon (type I pause), which leads to activation
956 of Rsh (step D). Rsh could also potentially be activated if free Rsh interacts with a stalled ribosome
957 downstream of the second codon (Type II pause) (step E), although its frequency could be limited
958 by relatively low abundance of such stalled complexes compared to the free 50S subunit.
959 Conditions inducing hibernating ribosomes, which are likely less accessible to Rsh, would

960 sequester ribosomes from the translation cycle and displace Rsh (step F), thereby rendering Rsh
961 labile in a Clp protease dependent manner (step G).
962
963
964
965
966
967

Figure 1

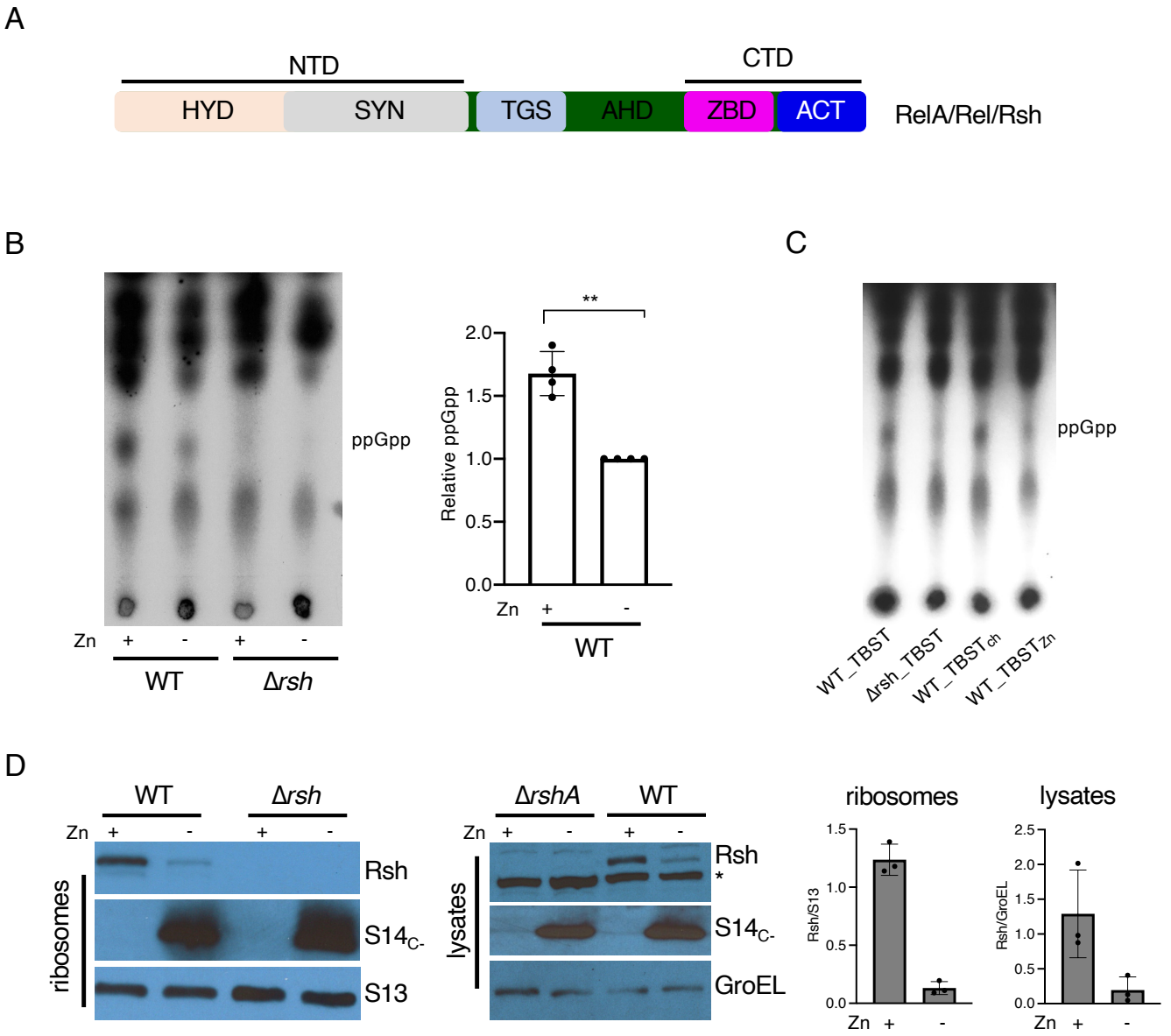
A
NTD
CTD
HYD
SYN
TGS
AHD
ZBD
ACT
RelA/Rel/Rsh
B
ppGpp
Zn + - + -
WT
Δrsh
Relative ppGpp
**
2.0
1.5
1.0
0.5
0.0
Zn + -
WT
C
ppGpp
WT_TBST
Δrsh_TBST
WT_TBST ch
WT_TBST Zn
D
WT
Δrsh
Zn + - + -
ribosomes
Rsh
S14C-
S13
ΔrshA
WT
Zn + - + -
lysates
Rsh
*
S14C-
GroEL
ribosomes
Rsh/S13
1.5
1.0
0.5
0.0
Zn + -
lysates
Rsh/GroEL
2.5
2.0
1.5
1.0
0.5
0.0
Zn + -

Figure 1: Attenuated stringent response and loss of Rsh in zinc-starved mycobacteria. A. A conserved domain architecture in mycobacterial RelA/SpoT homologue (Rsh) compared to RelA nd Rel in other species. The N-terminal domain (NTD) containing the hydrolase (HYD) and synthase (SYN) is distinguished from the C-terminal domain (CTD) by TGS (Thr-RS, GTPase and SpoT) and alpha-helix domain (AHD). The CTD is comprised of ZBD (zinc binding domain) and ACT (aspartokinase, chorismate mutase and TyrA) subdomains. **B.** Radio-TLC showing ppGpp levels in cultures of wild-type (WT) *M. smegmatis* isolated from high-zinc (1mM $ZnSO_4$) and low-zinc (1 μM TPEN) Sauton's medium after 96 hours of growth. ^{32}P-labeled sodium phosphate (100 μCi/mL) was added to the cultures six hours prior to starvation in TBST for three hours. After starvation nucleotides were extracted in formic acid and amounts equivalent to 50000 cpm were analyzed by TLC. Purified cold ppGpp was loaded as positional marker. The plot shows ppGpp levels in high-zinc WT samples relative to their low-zinc counterparts from four biologically independent experiments. **C.** Radio-TLC showing ppGpp levels in WT cells cultured for 96-hours in high-zinc Sauton's medium, then labelled for six hours, and resuspended in either TBST, or Chelex 100-treated TBST ($TBST_{ch}$), or zinc-supplemented $TBST_{ch}$ ($TBST_{Zn}$). A Δ*rsh* mutant was used as control in panels B and C. **D**. Immunoblot analysis of Rsh levels in 70S ribosomes purified from 96-hour-old high-and low-zinc cultures of *M. smegmatis* strains described in panel B. S14c- was used as a marker for the remodeled C- ribosome, while S13 was used as the loading control for ribosomes. In the set of immunoblots on the right, cell lysates from the samples used for ribosome analysis were probed. The asterisk indicates a non-specific unknown protein cross-reactive to Rsh antibody. The plots to the extreme right show the normalized average difference in Rsh between high- and low-zinc cultures from three independent experiments.

Figure 2

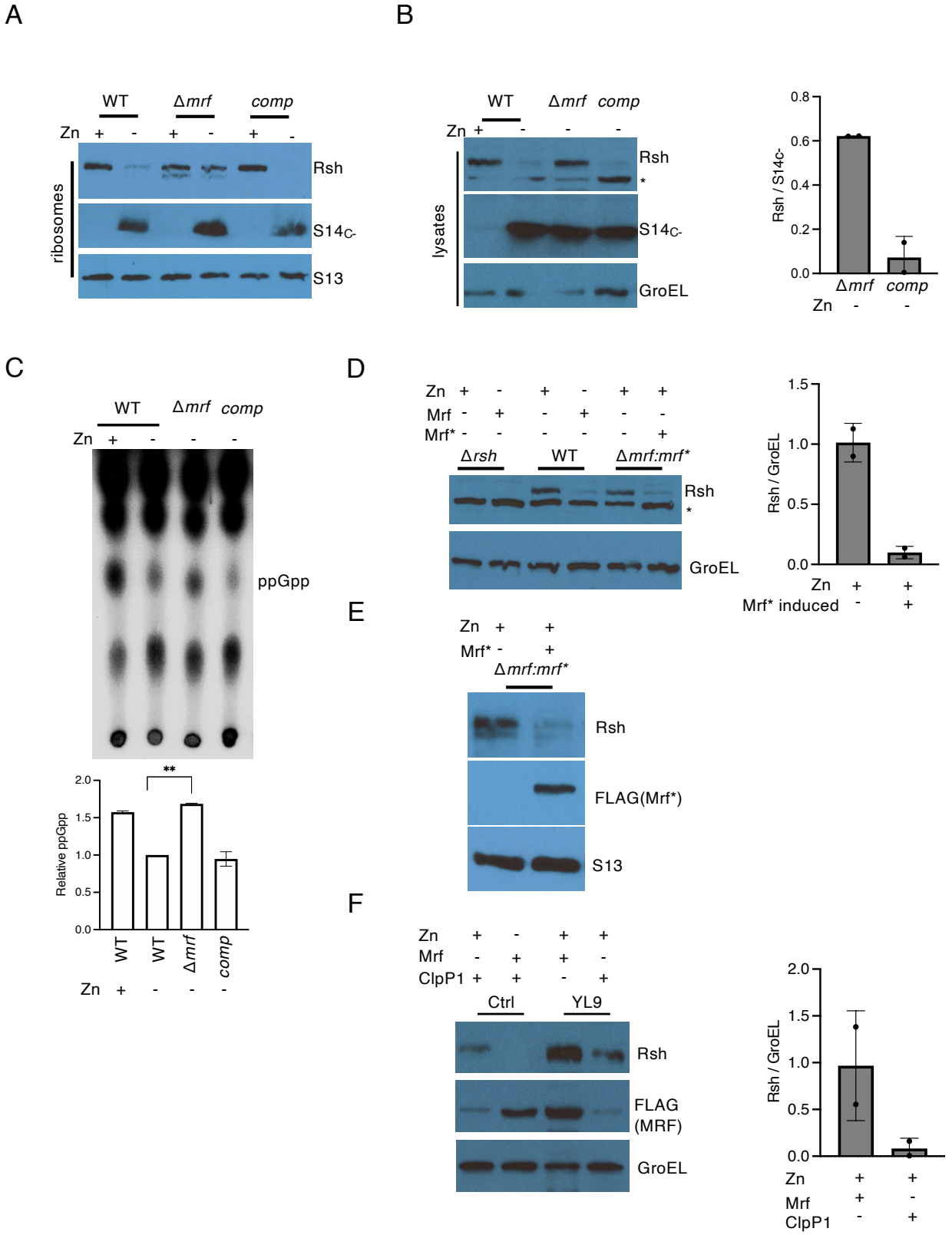
A
WT
Δmrf
comp
Zn + - + - + -
ribosomes
Rsh
S14C-
S13
B
WT
Δmrf
comp
Zn + - - -
lysates
Rsh
*
S14C-
GroEL
Rsh / S14c-
0.8
0.6
0.4
0.2
0.0
Δmrf
comp
Zn - -
C
WT
Δmrf
comp
Zn + - - -
ppGpp
Relative ppGpp
2.0
1.5
1.0
0.5
0.0
**
WT
WT
Δmrf
comp
Zn + - - -
D
Zn + - + - + +
Mrf - + - + - -
Mrf* - - - - - +
Δrsh
WT
Δmrf:mrf*
Rsh
*
GroEL
Rsh / GroEL
1.5
1.0
0.5
0.0
Zn + +
Mrf* induced - +
E
Zn + +
Mrf* - +
Δmrf:mrf*
Rsh
FLAG(Mrf*)
S13
F
Zn + - + +
Mrf - + + -
ClpP1 + + - +
Ctrl
YL9
Rsh
FLAG
(MRF)
GroEL
Rsh / GroEL
2.0
1.5
1.0
0.5
0.0
Zn + +
Mrf + -
ClpP1 - +

Figure 2: Mrf accumulation causes loss of Rsh. A-B. Analysis of Rsh in 70S ribosomes (A) and cell lysates (B) from high- or low-zinc cultures of Δ*mrf* and complemented (Δ*mrf*comp) strains of *M. smegmatis.* High and low-zinc cultures of WT were controls. $S14_{c-}$, S13 and GroEL were probed as loading controls for ribosomes or cell lysates as indicated. The asterisk in panel B indicates a non-specific protein cross-reactive to Rsh antibody. **C.** Radio-TLC showing ppGpp levels in 96-hour old high- or low-zinc cultures of WT and low-zinc cultures of Δ*mrf and* Δ*mrfcomp* of *M. smegmatis* strains after 3-hours of starvation in TBST. Purified cold ppGpp was loaded as positional marker. The plot shows relative ppGpp levels in each sample compared to the level in low-zinc culture of WT from two biologically independent experiments. **D.** Ectopic Mrf expression causes loss of Rsh. Levels of Rsh in the cell lysates of a *M. smegmatis* strain (pYL222) expressing FLAG-tagged Mrf* under the acetamide-inducible promoter. Cells were cultured in high-zinc Sauton's medium (1mM ZnSO4) containing 0.2% succinate as the carbon source until OD 0.6, after which Mrf* expression was induced with 0.2% acetamide, and cells were grown for 96 hours from inoculation. Uninduced cells were used as the reference. As controls, 96-hour old cells from the wildtype (WT) and Δ*rsh* strains cultured in either high- or low-zinc (1μM TPEN) Sauton's medium with succinate as the carbon source. The plot shows average normalized density of Rsh from two independent experiments. **E.** Analysis of Rsh in ribosomes purified from 96-hour-old induced or uninduced high-zinc cultures of pYL222 strain. **F.** Simultaneous accumulation of Rsh and Mrf in YL9 cells (Li et al. 2020) upon conditional depletion of ClpP1 protease. Cells were grown in high-zinc Sauton's medium until OD of 0.6, after which anhydrotetracycline (ATc) was added to induce CRISPRi system to deplete ClpP1. Cell lysates were analyzed after 16 hours of ClpP1 depletion. A parallel uninduced cells were used as control. YL9 cells grown for 96 hours in high- or low-zinc Sauton's medium without ATc were used as controll. The plot shows average normalized density of Rsh from two independent experiments.

Figure 3

A

```
Ec_RelA     QNRSKDNGRVVVEGVGNLMHHIARCCQPIPGDEIVGFITQGRGISVHRADCEQLAELRSH  647
Mtb_Rsh     RPRSTDDVGVSVPGAPGVLTKLAKCCTPVPGDVIMGFVTRGGGVSVHRTDCTNAASLQQ-  693
Msm_Rsh     RQRSNDDTGVAVPGAPGVLTKLAKCCTPVPGDTIMGFVTRGGGVSVHRTDCTNAESLQQ-  700
```

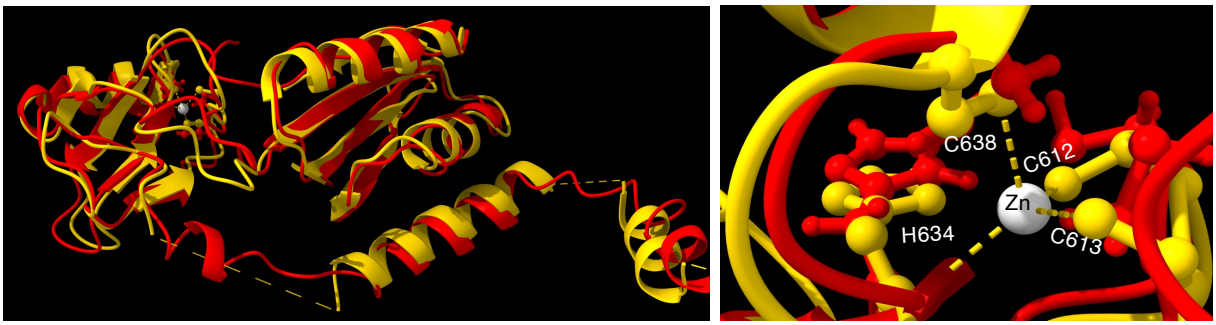

B

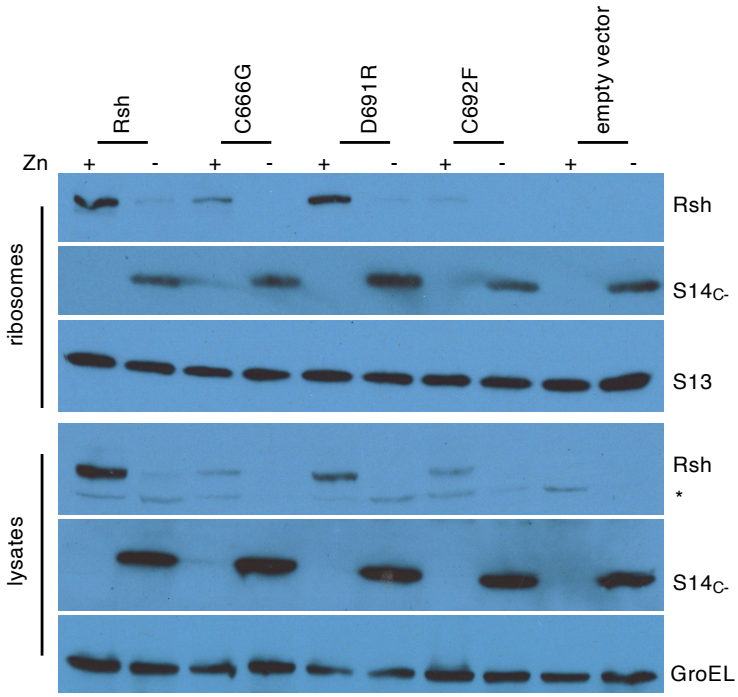

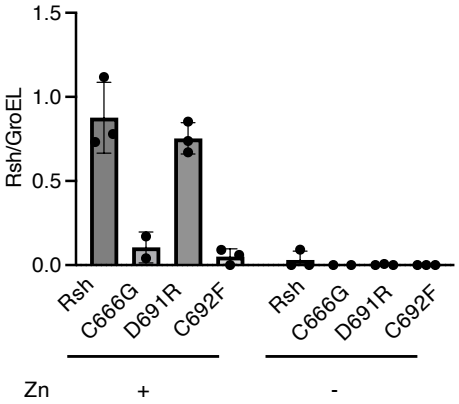

C

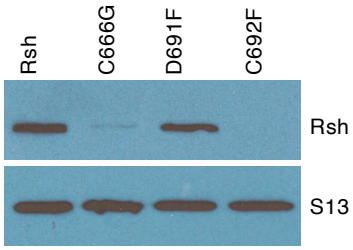

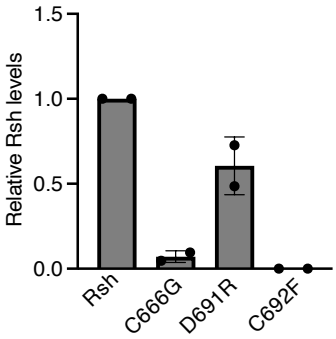

Figure 3: **Ribosome binding residues in Rsh are critical for its intracellular stability**. **A.** (Top) Sequence alignment of the C- terminal region of Rsh from *E. coli*, *M. smegmatis* and *M. tuberculosis* depicting the CCHC like zinc-finger (highlighted yellow) in the ZBD. (Bottom) Superimposition of the structure (PDBID: 5IQR) of the ZBD region from *E. coli* (yellow) and *M. smegmatis* (red). Zinc atom coordinated (shown with dashed lines) by the CCHC motif (shown as ball-and-stick model and numbered based on *E. coli* sequence) has been zoomed in the image to the right. The corresponding residues from *M. smegmatis* (shown in red ball-and-stick model) predict similarity in spatial orientation with respect to their *E. coli* counterparts. **B.** Immunoblot analysis of Rsh variants ($C_{666}G$, $D_{691}R$ and $C_{692}F$) in cell lysates and 70S ribosomes purified from 96-hour-old high-zinc cultures of a Δ*rsh* strain *of M. smegmatis* expressing each Rsh variant individually from an integrative plasmid (pYL238, pYL240, pYL241, pYL242 for Rsh, Rsh_{C666G}, Rsh_{D691R} and Rsh_{C692F}, respectively). Cultures of Δ*rsh* strain expressing WT Rsh were controls. Normalized average levels of Rsh and its variants in cell lysates from three independent experiments are shown in the plot. **C.** *In vitro* ribosome binding of recombinant Rsh and its variants. 2.4 picomoles of 70S ribosomes purified from a 96-hour old high-zinc culture of Δ*rsh* strain of *M. smegmatis* were mixed with 1.2 picomoles of Rsh or variant proteins (purified from recombinant *E. coli* harboring pYL243, pYL246, pYL247, pY248 for Rsh, Rsh_{C666F}, Rsh_{D691R} and Rsh_{C692F}, respectively) and the mixture was incubated for 30 minutes at 37 °C. The complex was separated by ultracentrifugation through a 32% sucrose cushion. S13 was probed as the loading control. The plot shows quantitative analysis of Rsh from two biologically independent experiments.

Figure 4

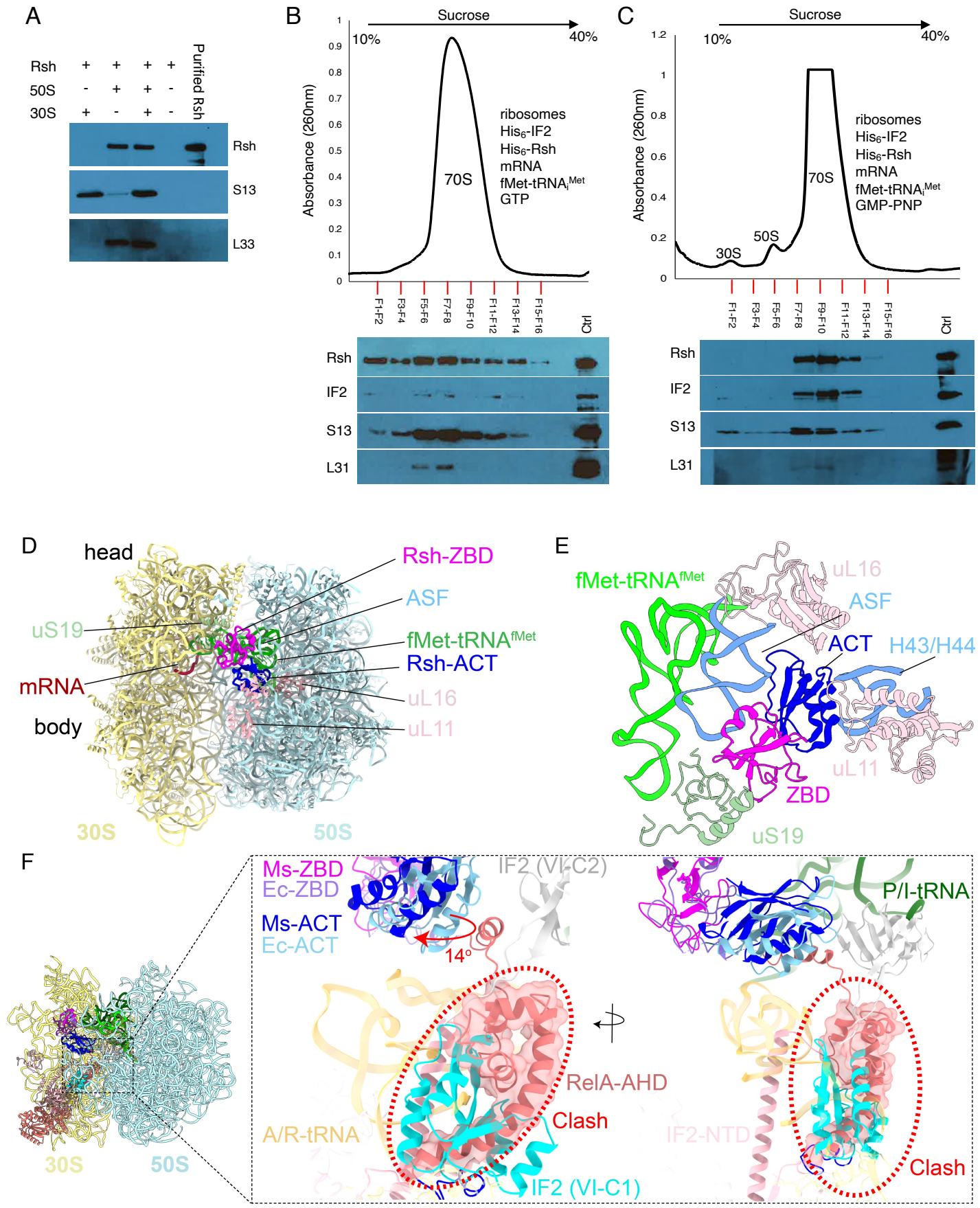
A
Rsh
50S
30S
Purified Rsh
Rsh
S13
L33
B
Sucrose
10%
40%
Absorbance (260nm)
70S
ribosomes
His6-IF2
His6-Rsh
mRNA
fMet-tRNAiMet
GTP
F1-F2
F3-F4
F5-F6
F7-F8
F9-F10
F11-F12
F13-F14
F15-F16
Ctl
Rsh
IF2
S13
L31
C
Sucrose
10%
40%
Absorbance (260nm)
30S
50S
70S
ribosomes
His6-IF2
His6-Rsh
mRNA
fMet-tRNAiMet
GMP-PNP
F1-F2
F3-F4
F5-F6
F7-F8
F9-F10
F11-F12
F13-F14
F15-F16
Ctl
Rsh
IF2
S13
L31
D
head
Rsh-ZBD
ASF
uS19
fMet-tRNAfMet
Rsh-ACT
mRNA
uL16
body
uL11
30S
50S
E
fMet-tRNAfMet
uL16
ASF
ACT
H43/H44
uL11
ZBD
uS19
F
Ms-ZBD
Ec-ZBD
IF2 (VI-C2)
P/I-tRNA
Ms-ACT
Ec-ACT
14°
RelA-AHD
Clash
A/R-tRNA
IF2-NTD
IF2 (VI-C1)
Clash
30S
50S

Figure 4: **Rsh interaction with a 70S translation initiation complex. A.** Co-sedimentation of Rsh with the 50S ribosomal subunit. Pellets resulting from ultracentrifugation on a 32% sucrose cushion were analyzed for S13 to confirm SSU, $L33_{C-}$ to confirm LSU, and Rsh to test preferential subunit binding. Rsh in the absence of ribosomes was included as control to rule out sedimentation of free protein. Purified Rsh was loaded as marker. **B-C.** Reconstitution of Rsh-bound pre-elongation complex in the presence of GTP (B) or GMP-PNP (C). Dissociated ribosomes (Figure S6) were mixed with indicated ligands in the presence of GTP or GMP-PNP. After incubation for 15 minutes in low-magnesium (1mM $MgCl_2$) buffer, recombinant Rsh was added, and magnesium was adjusted to 10 mM. The resulting mixture was incubated for additional 30 minutes. The complex was resolved in 10-40% SDG, and fractions corresponding to 70S-peak and its margin were analyzed for Rsh, IF2 and indicated ribosomal proteins by immunoblotting using anti-Rsh, anti-His_6 (for IF2), anti-S13 and anti-L31 antibodies. All reagents in the reactions in panels B and C were added in 5-fold molar excess relative to the ribosomal subunits. **D.** 2.7 Å resolution cryo-EM structure of the 70S-Rsh complex in late initiation state of translation, with a fMet-$tRNA_i^{Met}$ present in the P-site (green), mRNA (brown), and two C-terminal domains of Rsh, ZBD (magenta) and ACT (blue). The 30S and 50S subunits are shown in yellow and blue, respectively. **E**. Ribosomal components interacting with Rsh ZBD and ACT domain, along with the fMet-$tRNA_f^{Met}$ in the P-site (green), are shown. ZBD interacts with components of inter-subunit bridge B1a, uS19 (light green), and the A-site finger (ASF, sky blue). ACT interacts with the 50S components uL16 (sky blue), L11, and 23S rRNA helices H43/44 (sky blue). F. Superimposition of *M. smegmatis* 70S-Rsh, *E. coli* 70S-RelA (PDB ID: 5KPV) and *E. coli* 70S-IF2 (PDB ID: 6HTQ) structures, comparing their binding sites and conformations on the ribosome. Position of IF2 (VI-C1, cyan) suggests a direct steric clash (highlighted by red dotted circle) with the *E. coli* RelA's α-helical domain (RelA-AHD, light coral). *M. smegmatis* Rsh-ACT (Ms- ACT, blue) is rotated by ~14° (indicated by a red arrow) relative to the *E. coli* RelA-ACT (Ec-ACT, light blue), while the ZBD domains (Ms-ZBD, magenta and Ec-ZBD in light purple) have the same position.

Figure 5

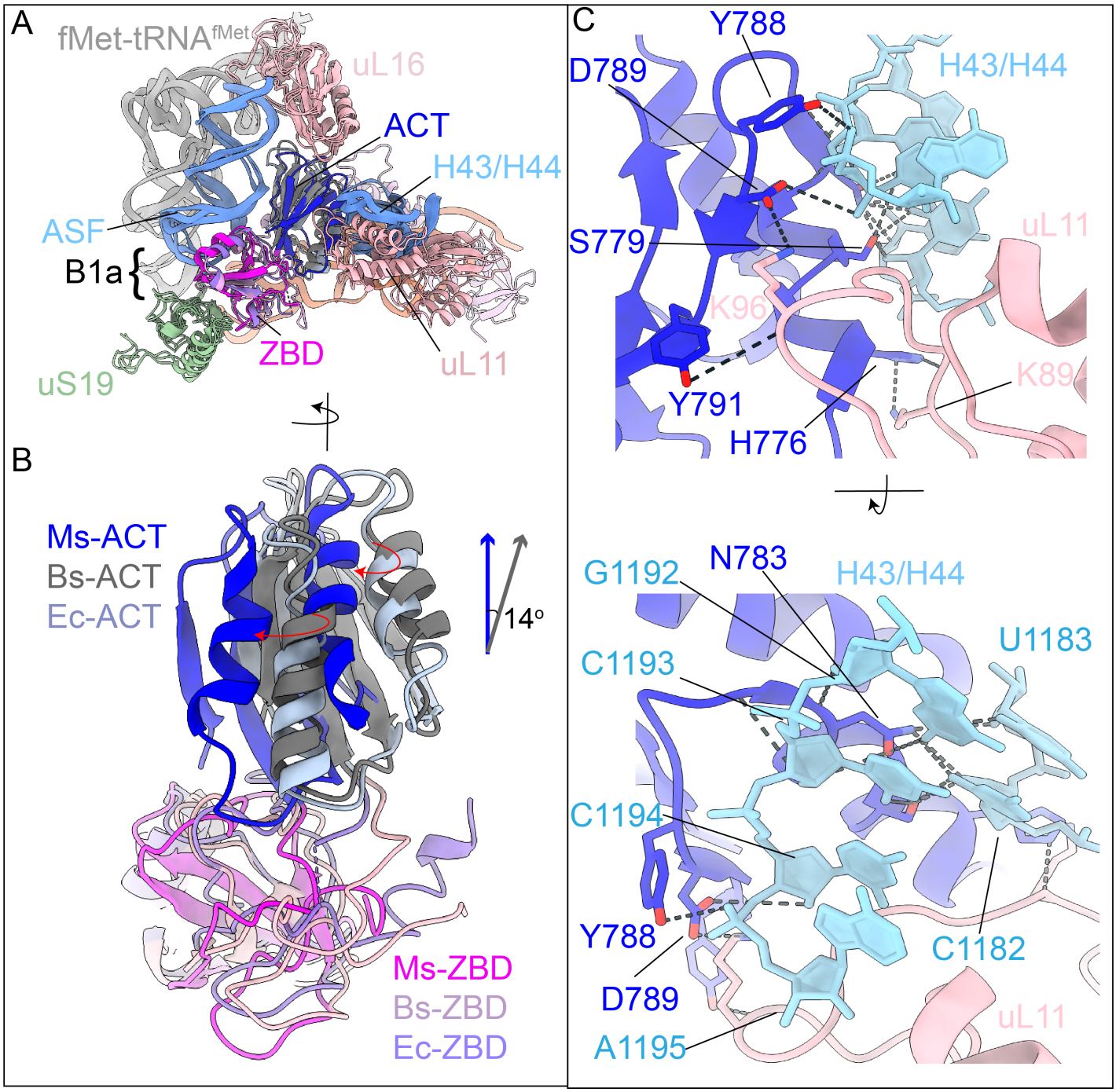
A
fMet-tRNAfMet
uL16
ACT
H43/H44
ASF
B1a
ZBD
uL11
uS19
B
Ms-ACT
Bs-ACT
Ec-ACT
14°
Ms-ZBD
Bs-ZBD
Ec-ZBD
C
Y788
D789
H43/H44
S779
uL11
K96
Y791
H776
K89
G1192
N783
H43/H44
U1183
C1193
C1194
Y788
C1182
D789
uL11
A1195

Figure 5: The Rsh-ACT domain interacts with the L7/L12 stalk base. A. Superimposition of the Rsh/Rel A interacting components from the 70S-Rsh/RelA complex structures from *M. smegmatis* (Ms) 70S-Rsh (ZBD, magenta; ACT, blue), *B. subtilis* (Bs) 70S-Rsh (ZBD, light pink; ACT, gray), and *E. coli* (Ec) 70S-RelA (ZBD, light purple; ACT, steel blue). Only components interacting with RelA/Rsh, L7/L12 stalk base (H43/H44 in blue), A-site finger (ASF in blue) uL16 and uL11 (light pink), the A/R tRNA (light coral) and uS19 (sea green), along with the P-site tRNA (light gray), are displayed. **B.** Superimposition of the C-terminal ZBD and ACT domain from Ms, Bs, and Ec (color-coded as in panel A) highlighting the rotation in Ms-ACT domain with respect to Ms-ZBD. **C.** Interactions of Ms Rsh-ACT (blue) with L11 (light pink) and the 23S rRNA helices H43/44 (light blue) are shown from two viewing directions.

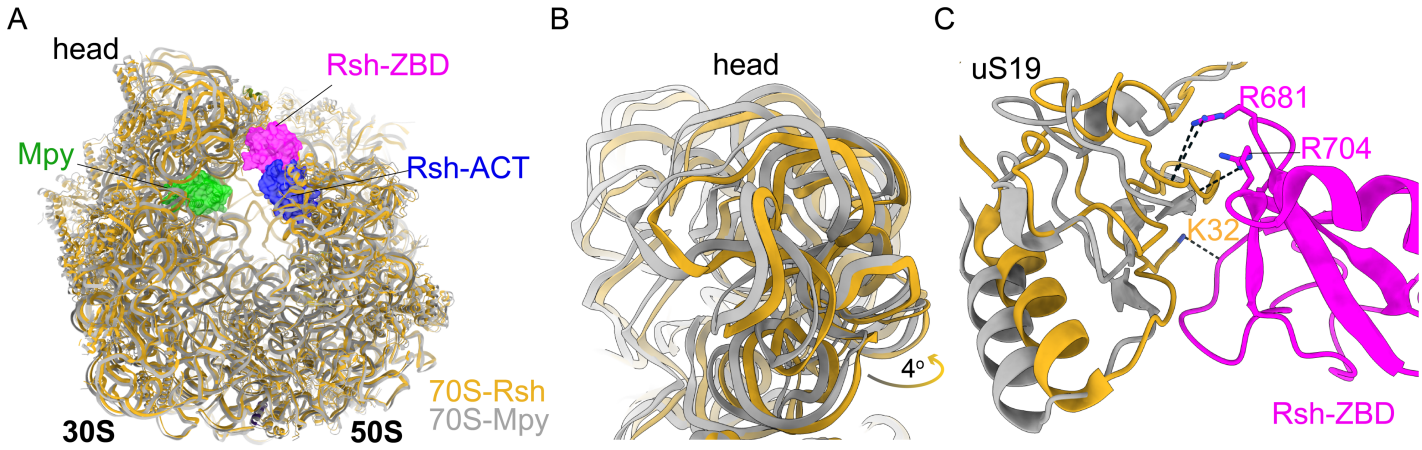

Figure 6: Structural basis of Rsh exclusion from a Mpy-bound 70S ribosome. A. Superimposition of Ms 70S-Mpy (gray, PDB ID:6DZI) and Ms 70S-Rsh (gold) structures. Rsh (ZBD, magenta; ACT, blue) and Mpy (green) are shown in the space-filled rendering. **B**. The 16S rRNAs corresponding to head domain of the 30S subunit in panel A has been enlarged to highlight their relative position in the two functional states. **C**. The position of uS19 (gray) in the Mpy-bound state would disrupt the observed interactions between Rsh-ZBD (magenta) and uS19 (orange).

Figure 7

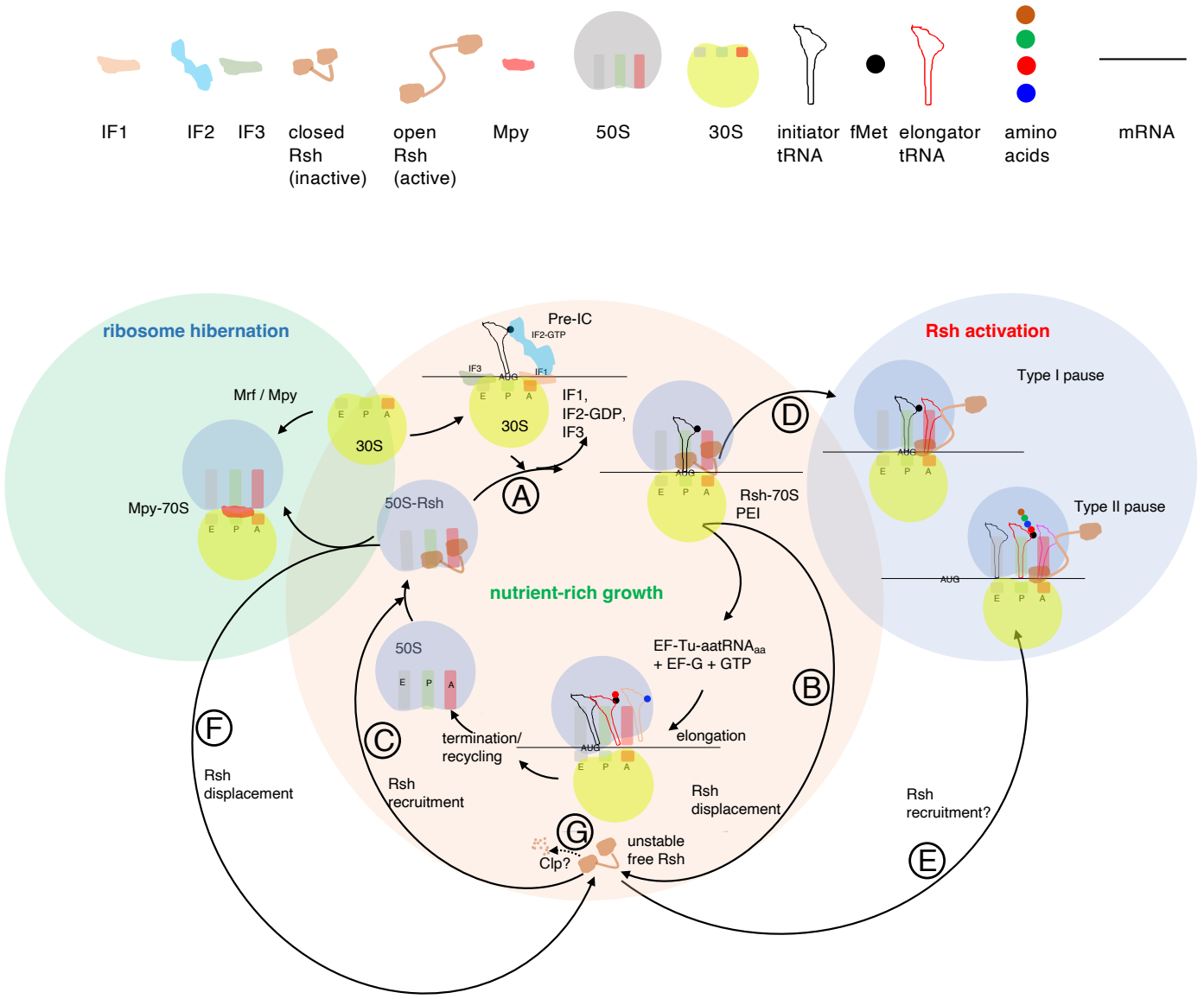

Figure 7: **Model of a dynamic interaction of Rsh with the ribosome in mycobacteria, influenced by three distinct conditions**. In a nutrient-rich condition supporting high translation activity, labile Rsh predominantly remains associated with the free 50S subunit, which confers stability to the protein. Rsh-50S complex joins with a 30S pre-initiation complex (pre-IC). Following the release of initiation factors, Rsh likely remains in the pre-elongation intermediate (PEI), which in an unrotated conformation is ready to elongate upon entry of the first A- site tRNA (step A). Rsh is likely sterically displaced during inter-subunit rotation associated with the first cycle of elongation (step B). Free Rsh associates with 50S subunit (step C) and the cycle continues until a deacylated tRNA enters the A-site at the second codon (type I pause), which leads to activation of Rsh (step D). Rsh could also potentially be activated if free Rsh interacts with a stalled ribosome downstream of the second codon (Type II pause) (step E), although its frequency could be limited by relatively low abundance of such stalled complexes compared to the free 50S subunit. Conditions inducing hibernating ribosomes, which are likely less accessible to Rsh, would sequester ribosomes from the translation cycle and displace Rsh (step F), thereby rendering Rsh labile in a Clp protease dependent manner (step G).

Supplementary materials

Figures S1-S10
Tables S1-S3

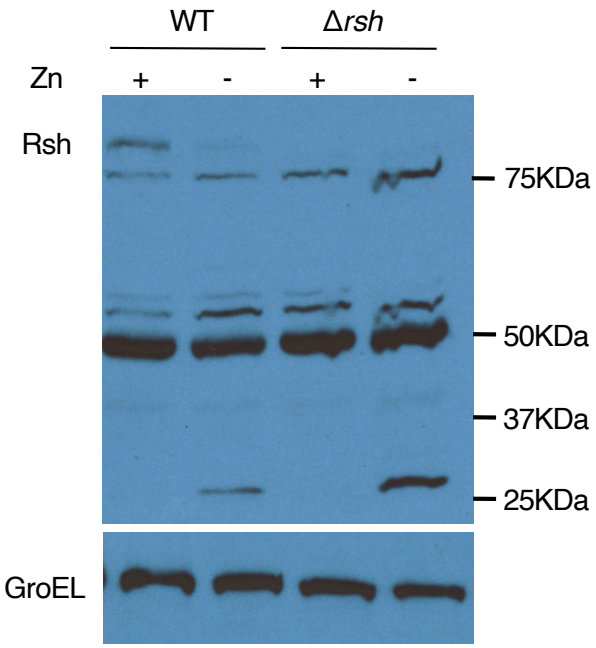

Figure S1: A full-gel immunoblot image of cells lysates from WT and Δ*rsh* strains cultured in high- (1mM $ZnSO_4$; abbreviated as Zn) and low-zinc Sauton's medium (1μM TPEN; abbreviated as T) and probed with anti-Rsh antibody. Data shows lack of any Rsh-derived smaller product in the low-zinc culture. GroEL from the lysate was probed as a loading control.

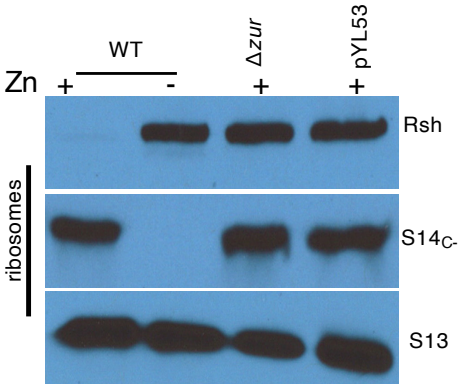

Figure S2: Ribosome remodeling has no effect on Rsh-ribosome interaction. Immunoblot analysis of Rsh bound to 70S ribosomes from 96-hour old high-zinc cultures of WT *M. smegmatis* and its two recombinant strains, Δ*zur* and Δ*c*-:pYL53, which constitutively expressed the remodeled (C-) ribosomes. Low-zinc culture of WT was used as control.

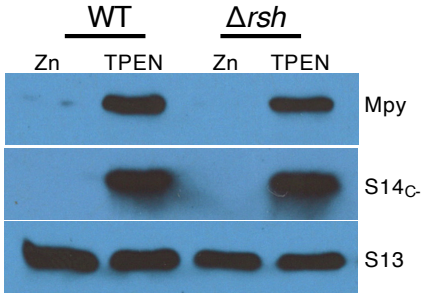

Figure S3: Levels of Mpy in 70S ribosomes purified from high- and low-zinc cultures of WT and Δ*rsh.* $S14_{c-}$ and S13 were probed as controls as indicated.

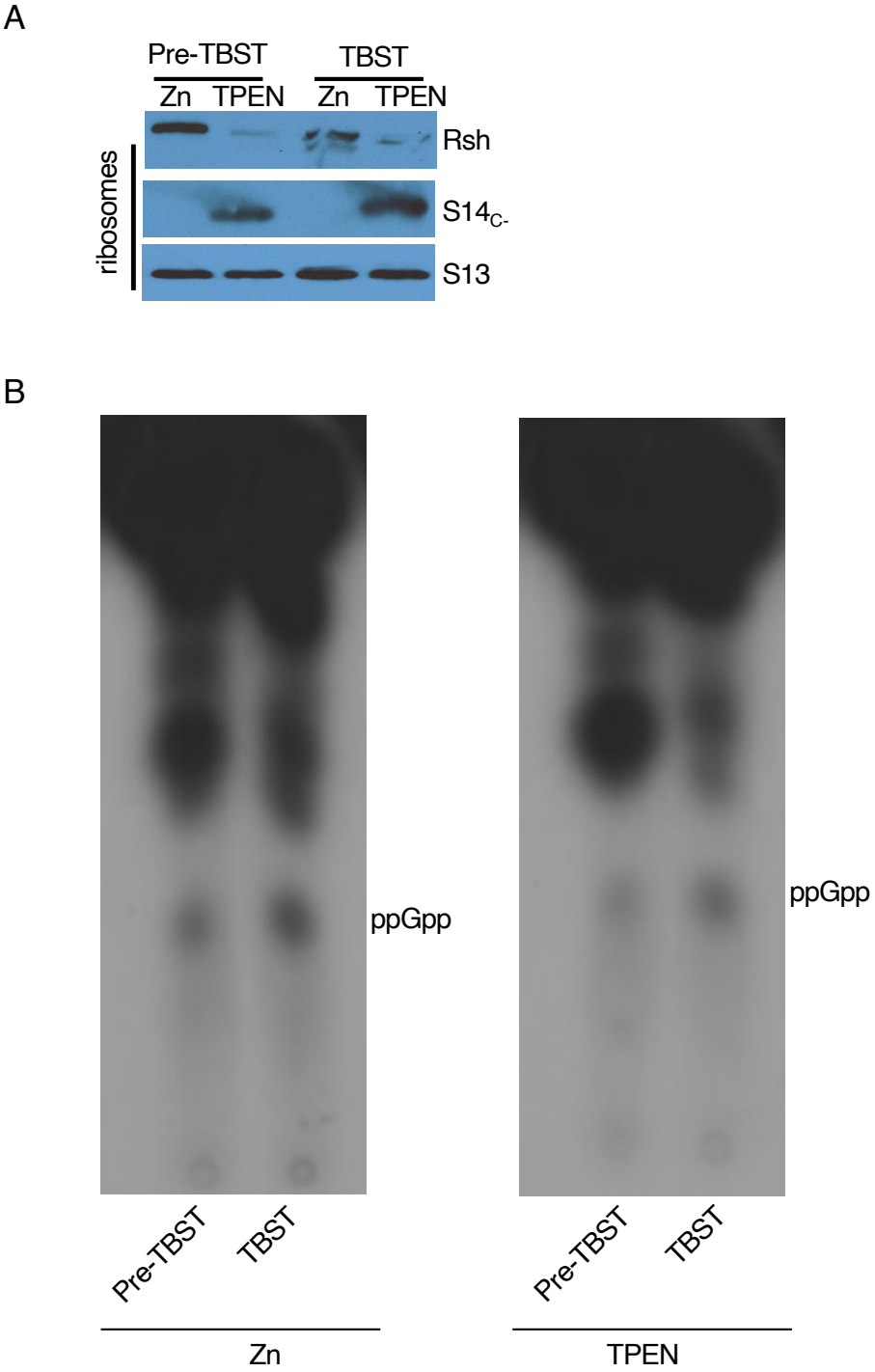

Figure S4: Level of Rsh-bound ribosomes (A) and ppGpp (B) in *M. smegmatis* before and after exposure to starvation (TBST) from high- or low-zinc culture conditions after 28 hours of growth.

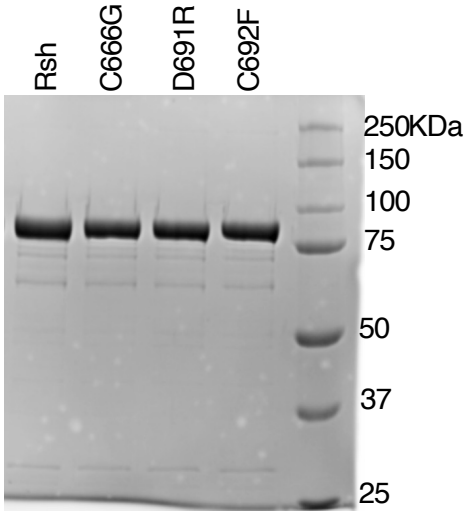

Figure S5: Purified recombinant 6xHis-tagged Rsh proteins expressed from an IPTG-inducible T7 promoter in the *E. coli* BL21 strain and visualized by SDS-PAGE and the Coomassie Blue stain. Each recombinant protein was purified from the same volume of starting cells using the same method, and equal volume of each sample was loaded on the gel.

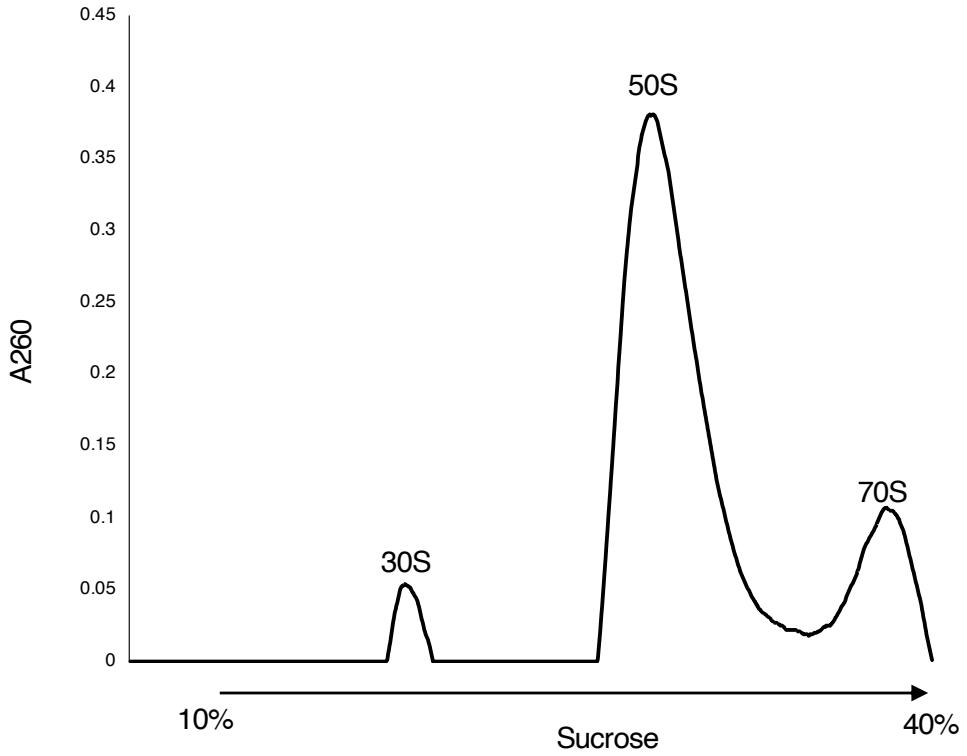

Figure S6: Sucrose density gradient profile of dissociated ribosomes used in the reconstitution experiments described in figures 4B and C. The reconstituted ribosome complex in figure 4C was used for structural studies.

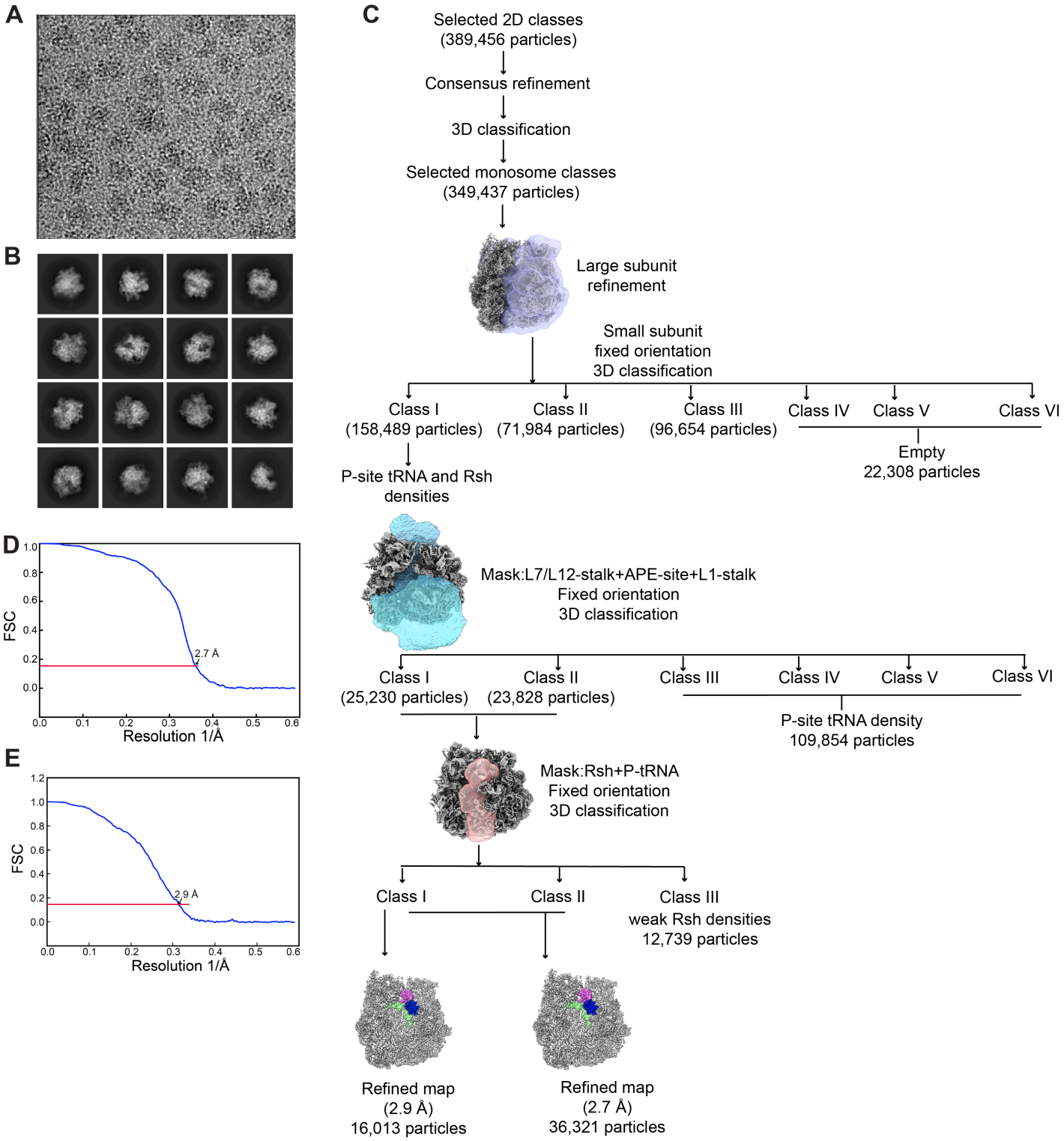

Figure S7: Image processing of M. smegmatis 70S-Rsh-fMet-tRNAiMet complex. A. A representative micrograph from the M. smegmatis 70S-Rsh-fMet-tRNAiMet complex dataset. **B.** Representative 2D class averages used for the 3D reconstructions. **C.** Flowchart showing the details of 3D classifications and refinements. **D.** Fourier-shell correlation (FSC) plot for the final map (36,321 particles) used in this study. Local resolution for this map is shown in figure S8. **E.** FSC plot for the map (16,013 particles) used in this study to model the Rsh-ACT domain.

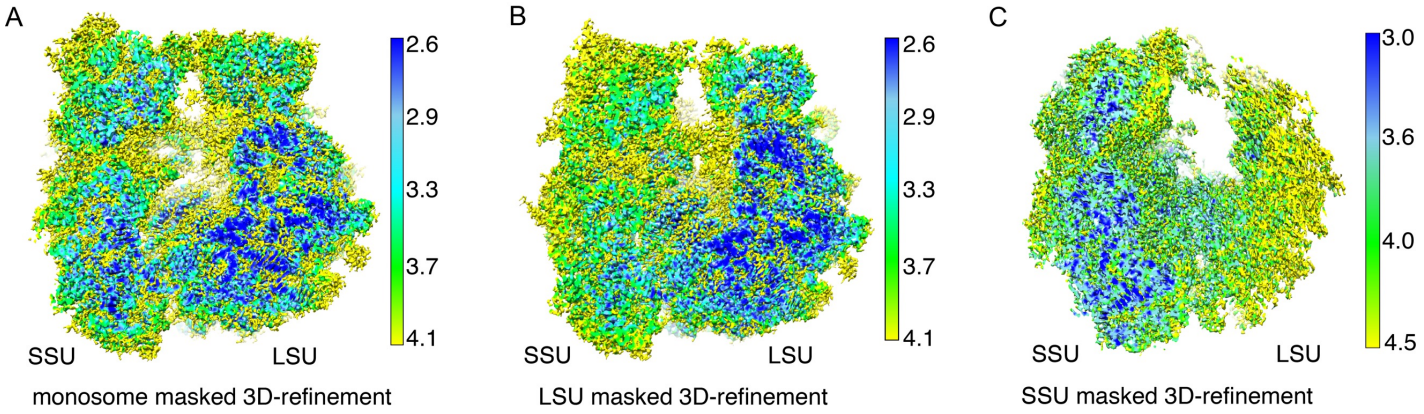

Figure S8: Local resolution of the cryo-EM map of the *M. smegmatis* 70S-Rsh-fMet-tRNAi^{Met} complex. Refined by using (A) 70S monosome, (B) 50S LSU, and (C) 30S SSU masks. In panels B and C, SSU and LSU appear to be partially disordered, as expected. A cutting plane has been applied to show the core of the ribosome in each case.

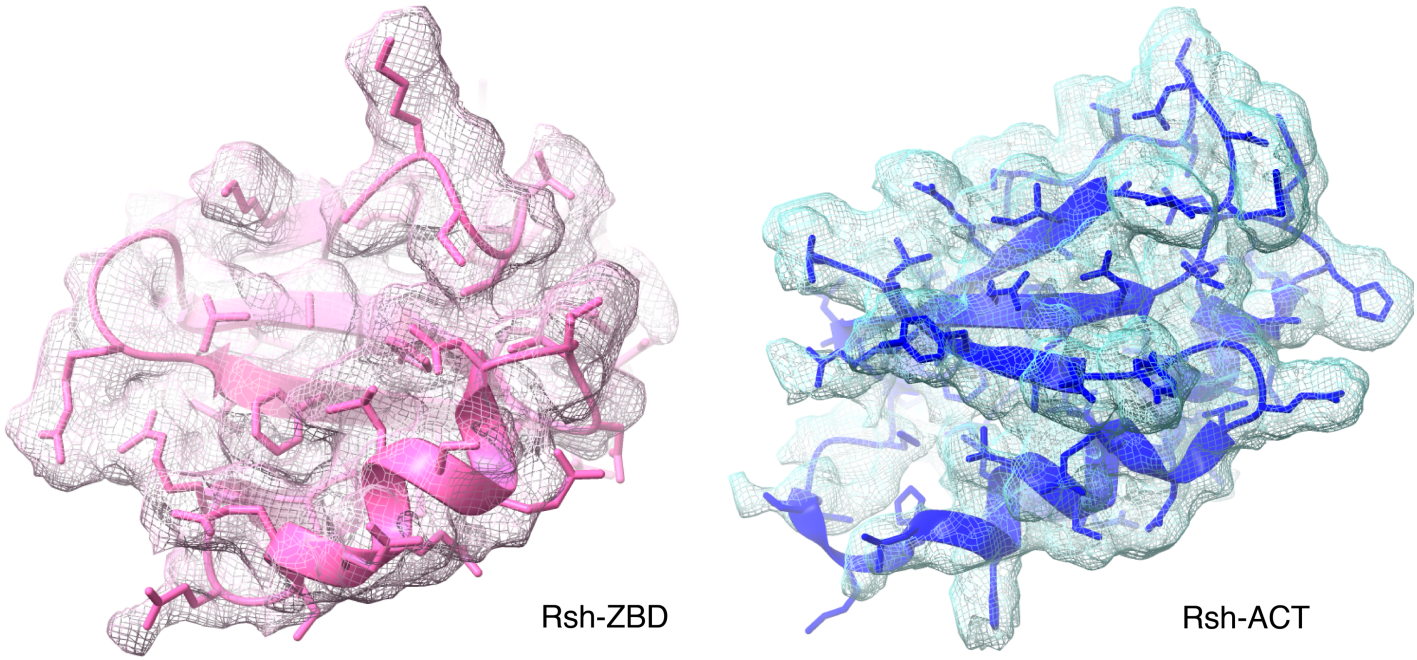

Figure S9: Modeling of the ZB- and ACT domains into corresponding cryo-EM densities. Two different density threshold values were used for modeling the two domains, as density for the main anchoring ZBD (pink) was stronger than that for the ACT domain.

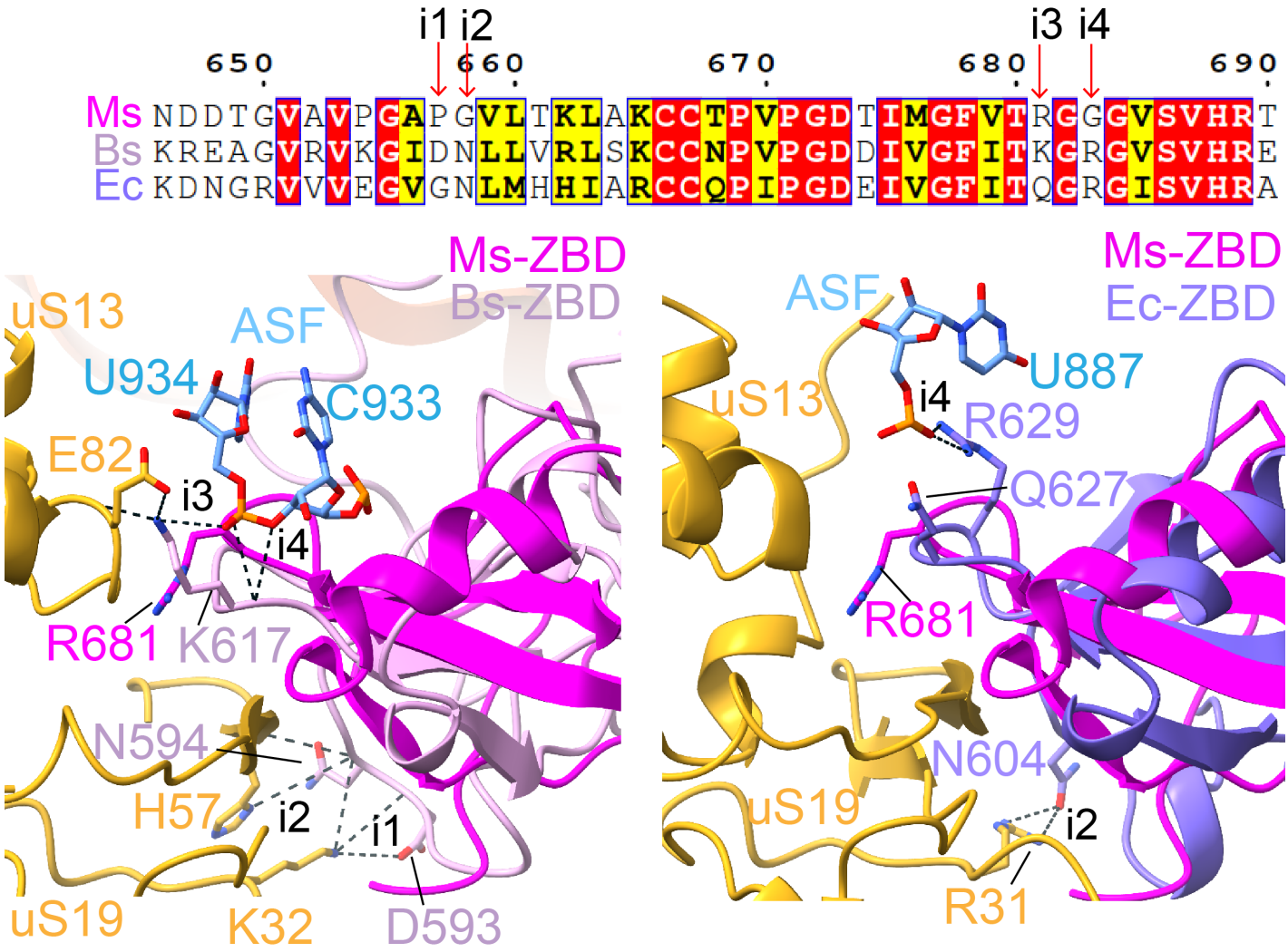

Figure S10: Species-specific differences in Rsh/RelA-ZBD interaction with uS19, uS13, and ASF. Top- Multiple sequence alignment of a short stretch in the ZBD domain of *M. smegmatis* (Ms) Rsh, *B. subtilis* (Bs) Rsh, and *E. coli* (Ec) RelA. Amino acid substitutions at four regions (indicated by red arrows) that result in species-specific differences in interactions (i1-i4) of the ZBD domain with ribosomal components. Bottom left- Superimposition of Ms 70S-Rsh (ZBD, magenta) and Bs 70S-Rsh (ZBD, light pink). Interactions of Bs-Rsh-ZBD with the ribosome that are absent in the case of Ms-Rsh-ZBD are displayed: two with uS19 (i1 and i2), one with uS13 (i3), and one with ASF (i4). Bottom right- Superimposition of Ms 70S-Rsh (ZBD, magenta) and Ec 70S-RelA (ZBD, light purple). Ec RelA-ZBD has two extra interactions with the ribosome, as compared to Ms Rsh-ZBD: One with uS19 (i2) and another with ASF (i4).

Table S1: List of plasmids and strains

Plasmids	Remarks	Reference
pJI37	P_{hsp60}-based expression vector for mycobacteria; *kan*^{r}	[1]
pMH94	L5-attp-based integrative vector for mycobacteria; *kan*^{r}	[1]
pYUB854	Cosmid vector, hygr	[1]
pTTPla	Tweety-attp-based integrative vector for mycobacteria; *kan*^{r}	[1]
pLam12	$P_{acatamidase}$-based expression vector for mycobacteria; *kan*^{r}	[1]
pJV53-SacB	Sucrose-sensitive marker SacB cloned in pJV53 @ SpeI site; *kan*^{r}	[1]
pET21b	Vectors carry an N-terminal T7-Tag sequence plus an optional C-terminal His Tag sequence, *amp*^{r}	[1]
pYL3	*kan*^{r} cassette in pMH94@EcoRV & NotI sites is replaced by *hyg*^{r} cassette from pYUB854; *hyg*^{r}	[2]
pYL40	*Msmeg_6069* internal deletion in pYL42 backbone @ SacI & XbaI, *hyg*^{r}	[1]
pYL53	MSMEG_6065-6070 cloned in pYL3 @ SacI+XbaI under a constitutive promoter (P^{const}): mutant variant of $P^{zur\text{-}box}$, *hyg*^{r}	[1]
pYL155	C-terminally FLAG-tagged *mrf* with P^{zurbox} cloned in pTTPla @ SacI & XbaI sites; *kan*^{r}	[1]
pYL181	C-terminally FLAG-tagged *mrf* with P^{zurbox} cloned in pYL180 @ SacI & XbaI sites; *apr*^{r}	[1]
pYL206	L5-attp-based integrative vector carrying tet-inducible dCas9 and gRNA complementary to Clpp1; *kan*^{r}	[1]
pYL222	*Msmeg_6069* with all six his/cys mutations (H to A, C to A) and Flag tag at C-terminal and $p^{zur\text{-}box}$ cloned in plam12 @ XbaI & HindIII sites; *kan*^{r}	This Study
pYL238	*MSMEG_2965* + 500 bp UPS cloned in pMH94 @ KpnI & XbaI; *kan*^{r}	This Study
pYL240	*MSMEG_2965* with C666G mutation + 500 bp UPS cloned in pMH94 @ KpnI & XbaI; *kan*^{r}	This Study
pYL241	*MSMEG_2965 with D691R mutation* + 500 bp UPS cloned in pMH94 @ KpnI & XbaI; *kan*^{r}	This Study
pYL242	*MSMEG_2965 with C692F mutation* + 500 bp UPS cloned in pMH94 @ KpnI & XbaI; *kan*^{r}	This study
pYL243	*MSMEG_2965* with N-terminal His-tag cloned in pET21b @ NdeI & HindIII; *amp*^{r}	This study
pYL246	*MSMEG_2965* (C666G) with N-terminal His-tag cloned in pET21b @ NdeI & HindIII; *amp*^{r}	This study
pYL247	*MSMEG_2965* (D691R) with N-terminal His-tag cloned in pET21b @ NdeI & HindIII; *amp*^{r}	This study
pYL248	*MSMEG_2965* (C692F) with N-terminal His-tag cloned in pET21b @ NdeI & HindIII; *amp*^{r}	This study
pYL259	*MSMEG_2965* + 500 bp UPS cloned in pYL3 @ KpnI & XbaI; *hyg*^{r}	This study
pYL260	*MSMEG_2965* (C666G)+ 500 bp UPS cloned in pYL3 @ KpnI & XbaI; *hyg*^{r}	This study
pYL261	*MSMEG_2965* (D691R)+ 500 bp UPS cloned in pYL3 @ KpnI & XbaI; *hyg*^{r}	This study
pYL262	*MSMEG_2965* (C692F)+ 500 bp UPS cloned in pYL3 @ KpnI & XbaI; *hyg*^{r}	This study
Strains	**Remarks**	**Reference**
mc²155 (WT)	High-Frequency Transformation strain of *M. smegmatis* as parent wild-type	[2]
Δ*msm*$_{c-}$	Unmarked Δ*Msmeg_6065-6070* in mc²155	[2]
Δ*mrf (YL1)*	Unmarked Δ*c*- operon harboring pYL40; *hyg*^{r}	[1]
Δ*mrf*comp (YL2)	Unmarked Δ*c*- operon harboring pYL40 and pYL155; *hyg*^{r}, *kan*^{r}	[1]
Δ*mpy* (YL3)	Unmarked Δ*Msmeg_1878* in mc²155	[2]
Δ*mpy*/Δ*mrf* (YL4)	Unmarked Δ*Msmeg_6065-6070*/Δ*Msmeg_1878* harboring pYL40; *zeo*^{r}, *hyg*^{r}	[1]
Δ*zur* (YL5)	Unmarked Δ*Msmeg_4487* in mc²155	[2]
Δ*zur*/Δmrf (YL6)	Unmarked Δ*Msmeg_6065-6070* /Δ*zur* harboring pYL40; *hyg*^{r}	[1]

YL9	Δ*zur* harboring pYL181 and pYL206; *apr*^{r}, *kan*^{r}	[1]
Δ*rsh*	Δ*Msmeg_2965* in mc^{2}155, *zeo*^{r}	This Study

1. Li Y, Corro JH, Palmer CD, Ojha AK: **Progression from remodeling to hibernation of ribosomes in zinc-starved mycobacteria**. *Proc Natl Acad Sci U S A* 2020, **117**(32):19528-19537.
2. Li Y, Sharma MR, Koripella RK, Yang Y, Kaushal PS, Lin Q, Wade JT, Gray TA, Derbyshire KM, Agrawal RK *et al*: **Zinc depletion induces ribosome hibernation in mycobacteria**. *Proc Natl Acad Sci U S A* 2018, **115**(32):8191-8196.

Table S2: List of oligonucleotides

Name	Sequence	Used in:
His1-R	GGTGCGGACGACGACAGCGCCGTCGAAGGTGGCGCTGACGAGCAGGGT	pYL222
His1-F	ACCCTGCTCGTCAGCGCCACCTTCGACGGCGCTGTCGTCGTCCGCACC	
His2-R	GGCCGAGACGGCTCCGGCCACCAGCTCAAGTAC	
His2-F	GTACTTGAGCTGGTGGCCGGAGCCGTCTCGGCC	
His3-R	CACGTCGGCGCGCCGGGCCAGACGGCGAAGCAGGAT	
His3-F	ATCCTGCTTCGCCGTCTGGCCCGGCGCGCCGACGTG	
p6069-CXXCR	ATCGTCACGCACGGTGGCCGAGACGGCTCCGTGCACCAGCTC	
p6069-CXXCF	GAGCTGGTGCACGGAGCCGTCTCGGCCACCGTGCGTGACGAT	
Pzurbox 6069-XF	CGCGCCGTTCGTCTAGACGCTGCACCAGTTCTCGCC	
p6069-FLAGHR	GGCCGGAAGCTTTCACTTATCGTCGTCATCCTTGTAATCCGATTGCTCTCCTGT	
pRelAMS-up500KpnIF	CTTCCCCGAACCGGTACCCCAGTTCAAGGACCTCAC	pYL236,240, 241,242,256, 259,260,261, 262
pRelAMS-XbaIFLAGR	CGAACCTCTAGATTACTTATCGTCGTCATCCTTGTAATCGGCCGCGCTGGTGA CGCG	
RelAC666G-F	ACCAAGCTGGCCAAGGGCTGCACCCCGGTGCCG	pYL240,246, 260
RelAC666G-R	CGGCACCGGGGTGCAGCCCTTGGCCAGCTTGGT	
RelAD691R-F	AGCGTGCACCGCACCCGTTGCACCAACGCCGAG	pYL241,247, 261
RelAD691R-R	CTCGGCGTTGGTGCAACGGGTGCGGTGCACGCT	
RelAC692F-F	GTGCACCGCACCGACTTCACCAACGCCGAGTCG	pYL242,248, 262
RelAC692F-R	CGACTCGGCGTTGGTGAAGTCGGTGCGGTGCAC	
prelA-NdeIHISF	TGACACATATGCACCACCACCACCACCACGTCGACGAGCCAGGCAAG	pYL243,246, 247,248
prelA-HindIIItgaR	CGCCGAACCGCTAAGCTTTCAGGCCGCGCTGGTGACGCG	

> Sequence of codon optimized synthetic IF2:

ATACGAGAACCATatgCACCACCACCACCACCACCAGGCACCGGTCGTGGGAGGGGTAAGACTTCCTCA
CGGTAACGGCGAGACGATCCGTCTGGCACGCGGCGCTTCATTATCAGATTTTGCTGAAAAGATAAATG
CGAATCCGGCTTCACTTGTGCAGGCATTGTTCAATCTTGGAGAAATGGTTACTGCCACGCAAAGTGTCG
GTGATGAAACACTTGAGCTGTTAGGGTCGGAGATGAATTACAATGTACAGGTCGTATCACCAGAAGACG
AGGACCGTGAATTGCTTGAAAGCTTTGATTTAACCTACGGCGAAGACGCGGGTGACGAGGAGGACTTA
GAGGTGCGTCCACCCGTTGTAACCGTTATGGGCCATGTCGATCATGGTAAGACTAGACTTCTGGACAC
AATCCGGAAGGCAAATGTGAGAGAGGGCGAGGCCGGCGGTATAACGCAGCACATCGGGGCCTATCAG
GTTGAGGTTGATTTGGACGGGACGGTGCGTCCCATAACTTTTATTGATACTCCCGGTCACGAGGCCTTT
ACCGCAATGCGTGCCAGAGGTGCCAAGGCTACAGATATTGCTATTTTAGTGGTAGCCGCGGATGATGG
CGTGATGCCTCAAACGGTTGAAGCGATTAACCACGCACAGGCCGCGGACGTTCCGATAGTGGTAGCA
GTCAACAAAATTGATAAGGAAGGAGCGGACCCCGCTAAAATTCGTGGGCAGTTAACAGAATATGGATTA
ATACCGGAAGAGTATGGCGGAGACACCATGTTTGTAGATATCAGTGCGAAACAGGGAACAAATATTGAA
GCATTATTAGAAGCAGTGATTCTTACCGCAGACGCCTCTTTAGATTTGCGTGCAAACCCCGATATGGAA
GCTCAGGGAGTCGCTATAGAAGCCCATCTTGACAGAGGTCGGGGTCCTGTTGCTACTGTATTGATACA
GCGCGGCACCCTTCGGGTTGGTGATTCCGTTGTTGCGGGTGACGCTTATGGGAGAGTCCGGAGAATG
ATCGATGAACATGGAGAGGACGTCGAAGAAGCATTGCCGTCTCGGCCGGTCCAGGTAGTTGGTTTCAC
CTCGGTACCCGGCGCTGGGGACAATTTTTTAGTTGTAGATGAAGATCGGATCGCGCGTCAAATCGCGG
ATCGCCGGTCAGCGCGTAAACGGAACGCCCTTGCTGCACGTAGTCGCAAACGGATCAGCTTGGAGGA
CTTAGACTCCGCCCTTAAAGAGACGTCGCAATTAAACCTTATATTAAAAGGAGACAACGCGGGGACAGT
TGAAGCACTGGAAGAGGCCTTAATGGGAATCCAGGTGGACGACGAGGTAGAACTGCGCGTCATCGAC
CGCGGTGTCGGAGGCGTCACAGAAACGAATGTAAACTTAGCAAGTGCCTCGGACGCGATTATCATTGG
TTTTAACGTCCGGGCTGAAGGAAAGGCGACTGAATTGGCTAATAGAGAAGGAGTTGAAATACGCTATTA
TTCTGTAATCTACCAGGCGATTGATGAAATTGAAGCAGCACTTAAAGGAATGCTGAAGCCTGTATACGA
AGAGAAGGAGCTTGGGCGTGCAGAAATACGTGCCATCTTCCGCAGTTCTAAGGTGGGCAATATAGCTG
GCTGCCTTGTCACATCAGGAATAATGCGCCGCAACGCTAAGGCCCGTTTATTAAGAGACAATGTAGTAG
TTGCACAGAATTTGACGGTAAGTAGTTTAAGACGCGAAAAGGATGACGTAACGGAAGTTCGTGATGGTT
ACGAGTGCGGACTGACCTTAACCTATAATGACATCAAAGAAGGTGACGTAATTGAGACTTATGAATTAG
TTGAAAAAGCGCGTACTtgaCTCGAGTGGCCGATCC

Table. S3 Data collection, Refinement and Model Validation parameters.

Description	**70S-Rsh-fMet-tRNA$_i^{Met}$ complex**
Data collection	
Microscope	FEI Titan Krios
Voltage (kV)	300
Pixel size (Å)	0.846
Defocus range (μm)	-1.50 to -2.50
Average e^- dose per image (e^-/ Å^2)	66.59
Particles (initial)	1,928,609
Particles (final)	36,321
FSC-threshold	0.143
Resolution (Å)	2.7
Map-sharpening B factor (Å^2) overall	-44.3
Refinement	
RMS deviations	
Bonds (Å)	0.005
Angles (^{o})	0.616
MolProbity score	2.09
Clash score	13.51
Rotamer outliers (%)	0.41
Ramachandran plot	
Outliers (%)	0.13
Allowed (%)	6.82
Favored (%)	93.05
RNA	
Correct sugar puckers (%)	99.24
Angle outliers (%)	0.00
Bond outliers (%)	0.00
Good backbone conformations (%)	78.98
Model composition	
RNA bases	4843
Protein residues	6299